SEGUE-2: Old Milky Way Stars Near and Far

Constance M. Rockosi[1] , Young Sun Lee[2] , Heather L. Morrison[3], Brian Yanny[4] , Jennifer A. Johnson[5,6] , Sara Lucatello[7] , Jennifer Sobeck[8] , Timothy C. Beers[9] , Carlos Allende Prieto[10,11] , Deokkeun An[12] , Dmitry Bizyaev[13,14] , Michael R. Blanton[15] , Luca Casagrande[16], Daniel J. Eisenstein[17] , Andrew Gould[5], James E. Gunn[18], Paul Harding[3], Inese I. Ivans[19], H. R. Jacobson[20] , William Janesh[3], Gillian R. Knapp[18] , Juna A. Kollmeier[21] , Sébastien Lépine[22] , Martín López-Corredoira[10,11] , Zhibo Ma[23], Heidi J. Newberg[24] , Kaike Pan[13] , Jakub Prchlik[3], Conor Sayers[8] , Katharine J. Schlesinger[16], Jennifer Simmerer[19], and David H. Weinberg[5,6]

[1] University of California Observatories and Department of Astronomy and Astrophysics, University of California Santa Cruz, Santa Cruz, CA 95064, USA
[2] Department of Astronomy & Space Science, Chungnam National University, Daejeon 34134, Republic of Korea
[3] Department of Astronomy, Case Western Reserve University, Cleveland, OH 44106, USA
[4] Fermi National Accelerator Laboratory, Batavia, IL 60510, USA
[5] Department of Astronomy, The Ohio State University, Columbus, OH 43210, USA
[6] Center for Cosmology and AstroParticle Physics, The Ohio State University, Columbus, OH 43210, USA
[7] Osservatorio Astronomico di Padova—INAF, Vicolo dell'Osservatorio 5, I-35122, Padova, Italy
[8] Department of Astronomy, University of Washington, Seattle, WA 98195, USA
[9] Department of Physics and JINA Center for the Evolution of the Elements, University of Notre Dame, South Bend, IN 46556, USA
[10] Instituto de Astrofísica de Canarias, E-38205 La Laguna, Tenerife, Spain
[11] Departamento de Astrofísica, Universidad de La Laguna (ULL), E-38206 La Laguna, Tenerife, Spain
[12] Department of Science Education, Ewha Womans University, 52 Ewhayeodae-gil, Seodaemun-gu, Seoul 03760, Republic of Korea
[13] Apache Point Observatory and New Mexico State University, P.O. Box 59, Sunspot, NM 88349-0059, USA
[14] Sternberg Astronomical Institute, Moscow State University, Moscow, Russia
[15] Center for Cosmology and Particle Physics, Department of Physics, New York University, 726 Broadway, Room 1005, New York, NY 10003, USA
[16] Research School of Astronomy & Astrophysics, Australian National University, Cotter Road, Weston Creek, ACT 2611, Australia
[17] Center for Astrophysics | Harvard & Smithsonian, 60 Garden Street, Cambridge, MA 02138, USA
[18] Department of Astrophysical Sciences, Princeton University, Princeton, NJ 08544, USA
[19] Department of Physics and Astronomy, University of Utah, 115 S. 1400 E., Salt Lake City, UT 84112, USA
[20] Massachusetts Institute of Technology, Kavli Institute for Astrophysics and Space Research, Cambridge, MA 02139, USA
[21] Observatories of the Carnegie Institution for Science, 813 Santa Barbara Street, Pasadena, CA 91101, USA
[22] Department of Physics & Astronomy, Georgia State University, Atlanta, GA, USA
[23] TBanic Data, 39 Jianwai Street, Bldg 15-1106, Beijing, People's Republic of China
[24] Department of Physics, Applied Physics and Astronomy, Rensselaer Polytechnic Institute, Troy, NY 12180, USA

Abstract

The Sloan Extension for Galactic Understanding and Exploration 2 (SEGUE-2) obtained 128,288 low-resolution spectra ($R \sim 1800$) of 118,958 unique stars in the first year of the Sloan Digital Sky Survey III (2008–2009). SEGUE-2 targeted prioritized distant halo tracers (blue horizontal-branch stars, K giants, and M giants) and metal-poor or kinematically hot populations. The main goal of SEGUE-2 was to target stars in the distant halo and measure their kinematics and chemical abundances to learn about the formation and evolution of the Milky Way. We present the SEGUE-2 field placement and target selection strategies. We discuss the success rate of the targeting based on the SEGUE-2 spectra and other spectroscopic and astrometric surveys. We describe the final SEGUE-2/SDSS-III improvements to the stellar parameter determinations based on the SEGUE Stellar Parameter Pipeline. We report a $(g - i)$ color−effective temperature relation calibrated to the IRFM. We evaluate the accuracy and uncertainties associated with these stellar parameters by comparing with fundamental parameters, a sample of high-resolution spectra of SEGUE stars analyzed homogeneously, stars in well-studied clusters, and stars observed in common by the APOGEE survey. The final SEGUE spectra, calibration data, and derived parameters described here were released in SDSS-III Data Release 9 and continue to be included in all subsequent SDSS Data Releases. Because of its faint limiting magnitude and emphasis on the distant halo, the public SEGUE-2 data remain an important resource for the spectroscopy of stars in the Milky Way.

1. Introduction

Spectroscopic observations of stars in old stellar populations are of fundamental importance for understanding the formation and evolution of the Milky Way and the cosmological history of galaxy formation. Recent years have seen several massive ($>10^5$ stars) spectroscopic surveys that have produced age, composition, and kinematic data charting the Galaxy's formation history back to early epochs: the buildup of mass and the mass density profile, the accretion, dynamical, and chemical history of the Galaxy, and the formation of the stellar populations.

This paper describes the Sloan Extension for Galactic Understanding and Exploration 2 (SEGUE-2), the spectroscopic survey of Galactic stars carried out by the Sloan Digital Sky Survey (SDSS) during the first year of SDSS-III. SEGUE-2 shifted emphasis from that of SEGUE-1 (Newberg et al. 2002; Yanny et al. 2009) to target stars in the outer Galactic halo.

Section 2 discusses other recent Galactic surveys and their major focus to put the motivating ideas behind SEGUE-2 in context. Section 3 begins the discussion of SEGUE-2 by summarizing the observing plan and choice of spectroscopic fields. The selection of the target stars, the criteria used, and the size and global properties of the final sample are summarized in Section 4. In addition to the new observations, SEGUE-2 updated the SEGUE Stellar Parameter Pipeline (SSPP) to improve the estimates of the stellar parameters [Fe/H],[25] $T_{\rm eff}$, and log g[26] for all stellar spectra obtained with the original SDSS spectrographs.[27] The updates to the SSPP, the new temperature scale, and the calibration of this scale are described in Section 5. The improved SSPP was run for all SDSS/ SEGUE stellar spectra (SDSS, SEGUE-1, and SEGUE-2) and the results released and made available as part of SDSS Data Release 9 (DR9, Ahn et al. 2012). The accuracy and precision of stellar parameters from the new SSPP are described in Section 6. Section 7 describes sources of incompleteness and bias in the spectroscopic samples and how they can be corrected.

The DR9 SSPP parameters have remained available, unchanged, in subsequent SDSS-III and SDSS-IV data releases. The radial velocity (RV) measurement pipeline for SEGUE-2 is unchanged from SEGUE-1, and the RV uncertainties as tabulated in Yanny et al. (2009) also describe the SEGUE-2 RV errors; see also Section 6 of this paper. The reduced stellar spectra, as well as all the raw data and calibration information, are also available as part of the SDSS data releases for use in independent analysis (e.g., Ludwig et al. 2008; Caffau et al. 2011). These data remain a resource for stellar spectroscopy as new imaging surveys and the next generation of spectroscopic surveys become available.

2. SEGUE-2 in Context

2.1. The Galactic Halo

Stars in the solar neighborhood have long been known to belong to more than one population. The classic study by Eggen et al. (1962) established two populations: low-metallicity, high-velocity dispersion stars identified with the Galactic halo and solar-metallicity, low-velocity dispersion stars associated with the disk, leading to a model in which the initial gravitational collapse produced low-metallicity old stars and the gas-rich rotating disk with continuing star formation. In this picture, the formation process created a centrally concentrated density distribution, high-velocity dispersion, and generally low metallicity for the halo stars. It is now

thought that halo formation was more complex, with the accretion of smaller (hence metal-poor) galaxies playing an important part (Searle & Zinn 1978; Ibata et al. 1994). The expected split between halo and disk in metallicity and kinematics led studies of the halo relying on solar neighborhood stars to select them to have low metallicity (e.g., Bond 1980; Beers et al. 1985, 1992; Norris et al. 1999; Chiba & Beers 2000) or hot kinematics (e.g., Ryan & Norris 1991; Carney et al. 1996).

The advent of sensitive detectors allowing much fainter stars to be observed, of accurate photometry for reliable color selection of stellar samples, of deep wide-field photometric surveys for the identification of very large, homogeneous samples over large spatial scales, and of multiobject spectral surveys have carried these investigations far out into the Galactic halo and demonstrated the presence of substantial substructure. Photometry in the SDSS Early Data Release (Stoughton et al. 2002) proved sufficiently accurate to separate halo main-sequence turnoff stars from those in the disk and thick disk by their bluer colors, making it possible to map the spatial substructure in the halo on large scales (Yanny et al. 2003). This motivated SEGUE (Yanny et al. 2009), carried out as part of SDSS-II, and has been extended by several other large surveys of stellar properties and kinematics. Dynamical time arguments and numerical simulations show that the coherence of accreted stars will be longer-lived kinematically than spatially and that accretion time, orbit, and mass ratios all affect where and when the accreted stars are deposited in the halo and how long the structures remain coherent (Helmi 2008; Johnston et al. 2008; Zolotov et al. 2009; Tissera et al. 2014; Karademir et al. 2019). Thus, the amount of substructure in the stellar halo varies with distance from the Galactic center (GC) and is sensitive to the accretion history. These simulations also predict that the metallicity distribution function (MDF) provides a crucial diagnostic of the accretion history of the Galactic halo. Johnston et al. (2008) describe the relationship between mass, accretion time, and chemical enrichment of stellar halo progenitors and find that mergers contribute more metal-rich stars to the halo. The Aquarius (Cooper et al. 2010) and Auriga (Monachesi et al. 2019) simulations show that a spiral galaxy's halo is a relic of its accretion history, with fewer accretion events leading to steeper metallicity gradients. In the FIRE simulations, El-Badry et al. (2018) find that the fraction of stars with formation redshifts greater than 5 is substantially greater in the outer halo and that the best way to find them is to search at high Galactic latitudes at distances greater than 10 kpc from the Sun. All of these motivate a spectroscopic survey of stars in the distant halo of the Milky Way.

2.2. Spectroscopic Surveys of the Galactic Halo

In this section, we list the main parameters of other large Milky Way halo surveys and summarize the complementary nature of SEGUE-2. Phase 1 of the Large Sky Area Multi-Object Fiber Spectroscopic Telescope (LAMOST) observed stars with spectral resolving power[28] $R \sim 1500$ with 4000 fibers per field (Zhao et al. 2012) and included high-latitude ($|b| > 30°$) fields targeting the Galactic halo to $r < 16.8$ and fainter stars in the northern and southern Galactic caps. Data Release 5, the end of LAMOST-1, contains spectra of 8.2 million stars (Luo et al. 2015). LAMOST-2 has added medium-

---

[25] We use the standard notation: $[X/Q] = \log_{10}N(X)_* - \log_{10}N(X)_\odot - \log_{10}N(Q)_* + \log_{10}N(Q)_\odot$, where N is the number density of atoms.
[26] The surface gravity of a star is reported as $\log_{10}g$, where $g = GM_*/R_*^2$ in cgs units.
[27] Hereafter, stellar spectra acquired with the original SDSS spectrographs are referred to as SDSS/SEGUE spectra when the details of their specific selection in SDSS, SEGUE-1, and SEGUE-2 are not important. In fall 2009, after the end of the SEGUE-2 observations, the spectrographs were upgraded for the BOSS survey (Smee et al. 2013).

[28] Resolving power R is defined as $\lambda/\delta\lambda$.

resolution ($R \sim 7500$) spectroscopy, and its Data Release 6 contains more than 9 million low-resolution and 1.3 million medium-resolution spectra (Luo et al. 2018).

The Radial Velocity Experiment (RAVE) used the 6DF spectrograph to obtain $R \sim 7500$ spectra of 130 stars per field with $9 < I < 12$. Designed as a precursor to Gaia spectroscopy, RAVE observed the same wavelength region as Gaia, around the 8550 Å Ca II triplet (Steinmetz et al. 2006). The complete sample, released in DR5, gives spectra, stellar parameters, RVs, and abundances for about 450,000 stars. The Gaia-ESO (Gilmore et al. 2012) and GALactic Archaeology with Hermes (GALAH; De Silva et al. 2015; Martell et al. 2017) survey strategies began a new era of surveys designed around the expectation of exquisitely accurate parallax and proper-motion data for nearby stars from Gaia. Their samples of halo stars are within a few kiloparsecs of the Sun. The Gaia-ESO stars were observed with the GIRAFFE and UVES spectrographs on VLT-Kueyen in two optical bands with $R \sim 18,000$ and 28,000 and, for the brighter stars, at $R \sim 45,000$. The GALAH survey uses no color selection, while the Gaia-ESO survey targets turnoff stars with 80% of the fibers and brighter red stars in the red clump with the remaining 20% (Stonkutė et al. 2016). The H3 Survey (Conroy et al. 2019a) also uses Gaia parallaxes to eliminate nearby stars in order to focus on the distant halo. The H3 observations use the medium-resolution ($R \sim 23,000$) Hectochelle spectrograph to observe in a single echelle order spanning 5150–5300 Å. The main H3 sample is selected in the magnitude range $15 < r < 18$ from the Pan-STARRS PS1 photometry with a Gaia parallax cut. There is also an H3 "high value" sample of luminous halo tracers. The H3 survey plans to measure stellar parameters and distances for $\sim 200,000$ stars.

SDSS-III (Eisenstein et al. 2011) and SDSS-IV (Blanton et al. 2017) included stellar observations obtained as calibration targets (Fernández-Alvar et al. 2016) and in ancillary programs (Dawson et al. 2013) using the upgraded BOSS spectrographs (Smee et al. 2013). SDSS-III featured the large-scale APOGEE-1 and APOGEE-2 surveys (Zasowski et al. 2013, 2017; Majewski et al. 2017). The APOGEE spectrographs (Wilson et al. 2019) observe 300 spectra per field at $R \sim 22,500$ in the H band and target intrinsically red stars, selected in the JHK_s bands, in the Galactic disk and bulge. The APOGEE observations at high latitudes target globular clusters and halo field stars.

These surveys generally sample nearby stars. Queiroz et al. (2018) find that for $|b| > 20°$, 99% of the GALAH DR1 stars are closer than 3.3 kpc and found the distance for the 99% fractions of other surveys as follows: 6.5 kpc (RAVE DR5), 9.7 kpc (Gaia-ESO DR3), and 15.4 kpc (APOGEE-SDSS DR14). SEGUE-2 is one of the four surveys of the third incarnation of SDSS, SDSS-III (Eisenstein et al. 2011), and is a continuation and extension of SEGUE-1 (Yanny et al. 2009). SEGUE-2 is focused on stars in the outer halo. Observing in dark time and at moderate resolution, to limiting magnitudes as faint as $g = 20$ for some target classes, SEGUE-2 was able to target distant halo stars out to more than 100 kpc and is complementary to the surveys described above.

2.3. The New Galactic Halo

The major results of these surveys, including SEGUE-1 and subsequently SEGUE-2, include discoveries of stellar streams and other substructure resulting from the tidal destruction of dwarf satellite galaxies; warps, flares, and waves in the Galactic disk; the demonstration that the Milky Way has accreted populations of different metallicity; the discovery of extremely metal-poor, almost always carbon-enhanced, stars; measurements of the Milky Way's mass distribution over a large radius range; the discovery of stars with speeds faster than the escape speed; and the likely remnants of the original disk, now found in the halo. Together, these results lead to a picture of the Galactic halo as formed by accretion events throughout the Galaxy's history, look back toward the "first stars" and early nucleosynthesis, provide a picture of star formation in the extreme environment of the GC, measure the effect of dark-matter substructure on the formation of the smallest galaxies, and give insight into galaxy formation and evolution at high redshifts. This picture of the Galactic halo is the motivation and context for SEGUE-2 spectroscopy in the distant halo.

Substructure: Among the first SDSS results, Newberg et al. (2002) found density enhancements associated with tidal tails from the Sagittarius dwarf galaxy (Mateo et al. 1998; Dohm-Palmer et al. 2001; Majewski et al. 2004), while Yanny et al. (2003) discovered the Monoceros ring, which may be the remains of another accreted satellite or part of a warped and flared outer disk (e.g., Helmi et al. 2003; Ibata et al. 2003; López-Corredoira & Molgó 2014; Xu et al. 2015). These results and others show that the Sagittarius dwarf galaxy is currently being accreted by the Galaxy, producing tidal tails that have been found to stretch to at least 50 kpc from the dwarf galaxy itself (Newberg et al. 2003; Starkenburg et al. 2009; Ruhland et al. 2011; Belokurov et al. 2014; Janesh et al. 2016). The ubiquity of tidal accretion in the halo is demonstrated by the SDSS "Field of Streams" image (Belokurov et al. 2006) and by the analysis of SDSS photometry of the halo by Bell et al. (2008) and de Jong et al. (2010). The analysis of halo substructure by Naidu et al. (2020) using Gaia and the H3 survey finds that the entire distant halo was built from accreted satellites. A recent discovery combining Gaia proper motions with SDSS/SEGUE spectroscopy is the Gaia-Enceladus "sausage" (GSE; Belokurov et al. 2018a; Helmi et al. 2018) containing stars from an early accretion event that dominates the nearby halo and is responsible for the chemical dichotomy of nearby halo stars (Nissen & Schuster 2010; Jackson-Jones et al. 2014; Hayes et al. 2018). This accretion event was also likely responsible for the formation of the "Splash" (Bonaca et al. 2017; Belokurov et al. 2020), stars with metallicities more typical of the thick disk that have, however, very low angular momentum, making them bona fide halo stars now. The heating of the Galaxy's original disk during the early accretion of GSE would result in their current occupation of the halo.

Stellar population gradients: There is observational evidence, though not always consistent, that the halo's composition and kinematics—net rotation and anisotropy—change as a function of Galactocentric distance (e.g., Sirko et al. 2004a; Carollo et al. 2007, 2010, 2011; Beers et al. 2012; An et al. 2013, 2015; Deason et al. 2013; Belokurov et al. 2018b; Cunningham et al. 2019; Lee et al. 2019; An & Beers 2020, 2021). To distances of 15–20 kpc, the stellar halo has been well characterized by in situ measurements (e.g., Carollo et al. 2007; Deason et al. 2013; Belokurov et al. 2018b; Yoon et al. 2018; Fernández-Alvar et al. 2019). An important goal of SEGUE-2 is a larger sample of halo stars at greater distances, especially stars for which we can combine proper-motion measurements with RVs and metallicities from spectroscopy (e.g., Hattori et al. 2017). The H3 Survey

spectroscopy reaches the distant halo, and using H3, Conroy et al. (2019b) find a mean $[Fe/H] = -1.2$ for the Milky Way halo with no metallicity gradient out to 100 kpc.

Mass of the Milky Way: Distant halo tracers, including globular clusters and dwarf galaxies, are key to establishing the total mass of the Galaxy (e.g., Gaia Collaboration et al. 2018), while its radial density profile can be traced by measuring the velocity dispersion or escape velocity at different distances (Battaglia et al. 2005; Xue et al. 2008; Deason et al. 2012; Taylor et al. 2016; Williams et al. 2017; Callingham et al. 2019). These measurements are essential for studies of the Galaxy in the contexts of galaxy evolution and cosmology (Abadi et al. 2010; Boylan-Kolchin et al. 2010; Wang et al. 2012) and to the analysis of the 6D motions of high-velocity stars in the tails of the velocity distribution and the local escape speed (e.g., Smith et al. 2007; Piffl et al. 2014; Monari et al. 2018).

High-velocity stars: There is a second origin for high-velocity stars, including stars moving at greater than the escape speed. Hills (1988) predicted that three-body interactions involving the supermassive black hole at the GC could inject stars into the Galaxy at speeds exceeding the escape speed. The first such star discovered (Brown et al. 2005) is a B-type star with an RV of 853 km s^{-1}. Additional early-type hypervelocity stars (HVS) have been found since then (Brown et al. 2014; Zheng et al. 2014). Kollmeier & Gould (2007) pointed out that if the stellar population in the GC region is similar to that of the local disk, there should be a detectable population of lower-mass HVS. Koposov et al. (2020) recently found an HVS of type A whose 3D orbit points to an origin in the GC. However, RV searches for lower-mass HVS have so far found no further candidates. This suggests that the properties of binary stars, or of the initial mass function, are different in the GC environment. Proper motions from Gaia have provided a new way to search for HVS candidates (e.g., de la Fuente Marcos & de la Fuente Marcos 2019; Du et al. 2019) and, when combined with RV and even chemical abundance data, can reveal whether a star is escaping and whether it originated in the GC (Boubert et al. 2018; Hawkins & Wyse 2018; Marchetti et al. 2019). Beyond Galactocentric distances of ~20 kpc, however, RVs remain the best way to identify candidate HVS (Kenyon et al. 2018).

Metal-poor stars: The most metal-poor stars in the halo offer the possibility of investigating the past history of nucleosynthesis. While metal-poor stars are not always the oldest stars (e.g., Tumlinson 2010; Starkenburg et al. 2017; El-Badry et al. 2018), they are chemically old and polluted by the nucleosynthesis products of fewer previous generations of stars. In particular, stars with extremely low metallicity ($[Fe/H] < -3$) are likely to be polluted only by the first generation of stars, offering the best information so far available on the masses, structure, and deaths of Population III stars (e.g., Beers & Christlieb 2005). However, these stars are very rare and cannot be distinguished from the far more numerous stars with $[Fe/H] \sim -2$ using broadband photometry alone (e.g., Beers et al. 1985; Ivezić et al. 2008; An et al. 2013; Schlaufman & Casey 2014; Casagrande et al. 2019), requiring spectroscopic observations of large samples.[29] Further, the most metal-poor stars, with $[Fe/H] < -3$, require high-dispersion spectroscopy

to detect the extremely weak lines and to separate interstellar and stellar Ca II absorption, particularly for warm stars. Observations of the smallish number of known very-metal-poor stars show that almost all are carbon rich (e.g., Beers & Christlieb 2005; Lee et al. 2013; Placco et al. 2014; Yoon et al. 2018), can have large overabundances of the *r*-process heavy elements (Sneden et al. 1996; Barklem et al. 2005; Lai et al. 2008; Li et al. 2015a; Hansen et al. 2018), have unexpected abundance trends for elements such as Cr and Co (McWilliam et al. 1995), and show large dispersions in the relative abundances of light elements such as O, Mg, and Ca (e.g., Cohen et al. 2013; Aoki et al. 2014; Li et al. 2015b).

The targeting and sky coverage philosophy of SEGUE-2 capitalizes on the capabilities of the Sloan Foundation Telescope and survey instrumentation: a wide field, broad wavelength coverage, efficient moderate-resolution spectrographs, the multiplex advantage of the optical fiber system, and high total throughput to cover a large angular area and reach the distant halo. The SEGUE-2 strategy of maximizing the volume sampled in the distant halo is aimed at understanding the formation of the Galaxy's stellar halo by in situ star formation and by accretion of dwarf galaxies. Details of the survey design are discussed in the next section.

3. Survey Design and Data

The SEGUE-2 survey used the 2.5 m Sloan Foundation Telescope (Gunn et al. 2006) and the two original Sloan Digital Sky Survey fiber spectrographs (Smee et al. 2013), as did SEGUE-1 and the SDSS. Each spectrograph has a red- and blue-optimized channel and acquires data for 320 of the 640 fibers in the 3° diameter spectroscopic field. The fibers are plugged into aluminum plates mounted at the telescope focal plane. A set of 640 spectra acquired simultaneously is hereafter referred to as a "plugplate" or "plate." The fibers are 180 μm in diameter, 3″ on the sky, and the spectrograph resolution is 2.8 Å at 5000 Å, or $R \sim 1800$. SEGUE-2, like SEGUE-1, is a magnitude-limited survey. Each set of 640 spectra is integrated to a signal-to-noise ratio (S/N) per angstrom of > 10, averaged across the *g*-filter bandpass, for targets $g < 19.5$. The S/N target was set by the lower limit for reliable stellar parameter determinations from the SSPP. This results in a consistent relation between S/N and magnitude over the survey for stars of similar spectral type.

SEGUE-2 observed for the first year of SDSS-III, from 2008 August through 2009 July. The survey obtained 128,288 spectra of 118,184 unique stars on 211 plates, 204 of which were unique and 7 repeated. Two of those 204 plates were specially designed for the open cluster Berkeley 29 to add to the sample of cluster stars from earlier SDSS data (see Section 5.4.2).

In SEGUE-2, the 640 fibers available for each plate were allocated to 10 different target categories, each with their own *ugriz* color, magnitude, and proper-motion limits. These are described in more detail in Section 4. The focus on obtaining spectra in the distant halo of the Galaxy was the primary consideration in deciding how to select the spectroscopic targets, as well as in planning the layout of the survey on the sky. A star near the old-population main-sequence turnoff has absolute magnitude $M_g \sim 4.0$ (An et al. 2008), so a turnoff star at apparent magnitude $g = 19.9$ is at a distance of 15 kpc. This is approximately the magnitude at which the sky and source flux are equal in the 3″ SDSS fibers. The bright limit of the

---

[29] Recent photometric survey efforts involving one or more narrowband filters have pushed the limiting metallicity achievable down to $[Fe/H] \sim -3.0$ to -3.5 (e.g., Huang et al. 2021).

SEGUE imaging blue, SDSS orange
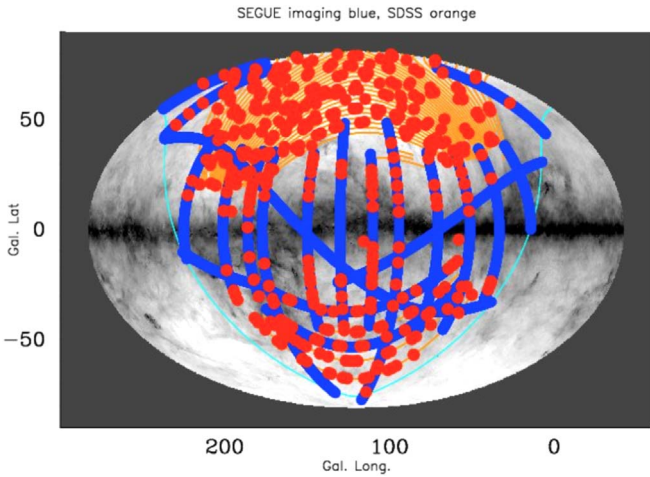
Figure 1. Layout of the SEGUE-1 and SEGUE-2 spectroscopy in Galactic coordinates in an Aitoff projection. The red circles are at the locations of the 7 deg^2 spectroscopic fields that comprise the SEGUE-1 and SEGUE-2 surveys. These are not to scale but show the SEGUE-2 field layout strategy of small overlapping groups of SEGUE-1 and SEGUE-2 fields to allow repeat observations of SEGUE-2 and SEGUE-1 targets. Each field has 640 spectroscopic targets. The orange stripes trace the original (contiguous) SDSS imaging survey area in the north Galactic sky. The blue stripes are the individual 2°.5 wide stripes of SDSS imaging data in the south Galactic cap, through the Galactic plane, and along known stellar streams that were taken in the SDSS and SDSS-II surveys. All the SEGUE-1 and SEGUE-2 spectroscopic targets were selected from the SDSS imaging data. The grayscale background is the Schlegel et al. (1998) dust extinction map.

SDSS imaging data is about 14th magnitude in the g, r, and i filters and sets the bright limit for the spectroscopic targets. The faint spectroscopic limit at $g = 19.5$ was chosen as a compromise between survey depth, S/N, and exposure time per plate. Given these magnitude limits, obtaining spectra for stars more distant than 15 kpc requires targeting stars more intrinsically luminous than the main sequence. For an old stellar population such as the halo, the choices are blue horizontal-branch (BHB) stars and red giants; SEGUE-2 targets both. Because these are short phases late in stellar evolution, the number of these stars in any population is small and the projected density on the sky low. The BHB stars and red giants that can be selected most efficiently using *ugriz* imaging (see Section 4) have projected densities much less than 100 per square degree at $g < 19.5$ for Galactic latitudes that avoid the disk. Therefore, maximizing the survey area in order to target as many of these rare tracers as possible was the highest priority when planning the layout of the plates on the sky. The distribution of the SDSS imaging area on the sky, from which the targets were selected, the time limit of one year, and the need to observe near the meridian (because there is no atmospheric dispersion correction over the 3° diameter field) were also important practical constraints. The final layout of the SEGUE-2 survey is shown in Figure 1. In contrast to the bright and faint plates of SEGUE-1, each SEGUE-2 field is covered by only one plate of 640 spectra. Where possible the plates were placed such that there was a small overlap with other SEGUE-2 plates or existing SEGUE-1 data to obtain repeat observations of about 10 stars per plate as a check on the RV zero points and other measurement accuracy.

The average projected stellar density in the magnitude range $14 < g < 19.5$ is much greater than the available fiber density. The desire to maximize the area and the constraint of limited observing time over only one year all but eliminated return

visits to any field. Therefore, SEGUE-2 acquired spectra for only a subsample of the stars in any field. The projected stellar density varies by factors of several over the SDSS imaging footprint, making the subsampling fraction different for every SEGUE field. This mismatch between the variable stellar density and the fixed number of fibers per field requires that investigations to measure the distribution function of a Galactic stellar population, or that otherwise require knowing the true density of a population or stellar tracer, must correct for this sampling factor as described in Section 7. It may also be necessary to account for the color, magnitude, and proper-motion selection of the tracer, also described in Section 7. The need to account for the survey sampling is a direct consequence of the priority put on a large survey area to maximize the number of distant halo tracers in limited observing time.

The imaging and astrometric data used to select targets, as well as the spectrographs and the fiber system, were the same for both SEGUE-1 and SEGUE-2, and both surveys were processed with the same software pipelines for Data Releases 8 and 9. Except for the specific selection used for the different kinds of spectroscopic targets, the data from the SEGUE-1 and SEGUE-2 surveys are otherwise very similar. Combining data from the two surveys in the analysis is no different than combining the different kinds of spectroscopic target types from one of the two surveys.

4. SEGUE-2 Spectroscopic Samples: Target Selection and Verification

The SEGUE-2 spectroscopic targets are selected from pre-DR8 SDSS photometry (hereafter SEGUE-2 photometry) because the SEGUE-2 targeting had to be complete before the final DR8 photometry was available. This target photometry is included in the public SDSS data for the specific areas of sky with SEGUE-2 spectroscopic observations and can be found in the SDSS database in the sppTargets table. The sppTargets table identifies all stars in the areas targeted by SEGUE-2 that passed the target selection criteria (as determined using the SEGUE-2 photometry) as well as the stars actually observed. In addition, the SEGUE-1 and SEGUE-2 target selection information is available for the final DR8 photometry over the entire SDSS imaging area. This full-footprint targeting information for DR8 is in the segueTargetAll table in the SDSS database. Using the target selection information and target photometry is discussed further in Section 7.

Some SEGUE-2 target categories used proper-motion information, either to select stars likely to have large space velocities or to remove local dwarf stars that contaminate the color and magnitude selection of more distant objects. As Gaia data were not yet available, the proper motions used to select SEGUE-2 targets were from the USNO-B proper-motion catalog (Monet et al. 2003), recalibrated as described in Munn et al. (2004), and available with DR7 and all subsequent data releases. All target categories that used proper-motion information selected only those objects with reliable proper-motion estimates, as in Kilic et al. (2006) (see footnote to Table 1). The errors of the recalibrated USNO-B catalog are ∼4 mas per coordinate (Munn et al. 2004). At a distance of 2 kpc, this is a transverse velocity error of ∼38 km s^{-1} per coordinate. The SEGUE-2 targets were selected using the DR7 version of the USNO-B proper motions, so are not affected by the systematic astrometric errors in DR8, which were resolved for

Table 1
SEGUE-2 Selection by Target Type

Target Class	Bit Name	Binary Digit	Selection Criteria[a]	Total[b]
Main-sequence Turnoff	SEGUE2_MSTO	0	$18 < g < 19.5$ $0.1 < (g-r) < 0.48$ psfmagErr$(g, r, i) < 0.05$	39,493
Red K Giants	SEGUE2_RKG	1	$15.5 < g < 18.5$ $r > 15$ $0.8 < (g-r) < 1.3$ $(u-g) > 0.84(g-r) + 1.758$ $(u-g) < 2.4(g-r) + 0.73$ psfmagErr$(g, r, i) < 0.05$ PMtotal < 11 mas yr^{-1} good PM[c]	1391
l-color K Giants	SEGUE2_LKG	2	$15.5 < g < 18.5$ $r > 15$ $0.7 < (u-g) < 3$ $0.5 < (g-r) < 0.8$ $0.1 < (r-i) < 0.6$ l-color > 0.09[d] psfmagErr$(g, r, i) < 0.05$ PMtotal < 11 mas yr^{-1} good PM[c]	23,891
Proper-motion K Giants	SEGUE2_PMKG	3	$15.5 < g < 18.5$ $r > 15$ $0.8 < (u-g) < 1.2$ $(u-g) > 2.375(g-r) - 0.45$ $(u-g) < 0.84(g-r) + 1.758$ psfmagErr$(g, r, i) < 0.05$ PMtotal < 7 mas yr^{-1} good PM[c]	17,978
Low-metallicity Candidate	SEGUE2_LM	4	$15.5 < g < 18$ $0.5 < (u-g) < 2.0$ $r > 15$ $0.3 < (g-r) < 0.8$ l-color > 0.115[d] psfmagErr$(g, r, i) < 0.05$ psfmagErr$(u) < 0.2$	16,507
Hypervelocity Star	SEGUE2_HVS	5	$17 < g < 20$ $V_{\rm tot} > 400$ km s^{-1} PMtotal > 8 mas yr^{-1} good PM[c] EITHER: $\mu_\perp < 6$ mas yr^{-1} OR $V_\perp > 400$ km s^{-1} EITHER: $0.35 < (g-r)_0 < 0.40$ AND $0.375 < (u-g)_0 - 2.5(g-r)_0 < 0.525$ OR $0.40 < (g-r)_0 < 0.60$ AND $0.225 < (u-g)_0 - 2.5(g-r)_0 < 0.425$	581
Extreme M Subdwarf	SEGUE2_XDM	6	$g > 15.5$ $(g-r) > 1.4$ $(r-i) > 0.4$ $15 < r < 20$ $(r-i) < 3.0(g-r) - 3.5$ PMtotal > 10 mas yr^{-1} $H_r > 10.0 + 2.5(g-r)$ [e] psfmagErr$(r, i) < 0.05$ good PM[c]	10,691
M Giant	SEGUE_MII	7	$15.5 < g < 19.25$ $i > 14.5$ $(u-g) > 1.8 + 0.9(g-r)$	638

Table 1
(Continued)

Target Class	Bit Name	Binary Digit	Selection Criteria[a]	Total[b]
			$(g - r) > 1.3$	
			psfmagErr$(g, r) < 0.05$	
			PMtotal < 11 mas yr^{-1}	
			good PM[c]	
High-velocity Halo Star	SEGUE2_HHV	8	$17 < g < 20$	4297
			$0.1 < (g - r) < 0.48$	
			$V_{\tan} > 300$ km s^{-1}	
			$V_{\tan} / \sigma(V_{\tan}) > 3.0$	
			good PM[c]	
Blue Horizontal Branch	SEGUE2_BHB	13	$15.5 < g < 20.3$	10,660
			$-0.5 < (g - r) < 0.1$	
			$0.8 < (u - g) < 1.5$	

Notes.
[a] Recall that all target selection is made with dereddened magnitudes, as described in Section 4.
[b] Total number of spectra of stars with this targeting bit set, including duplicate observations. Stars may have more than one targeting bit set.
[c] Acceptance criteria for data in SDSS/USNO-B catalog: (1) Match = 1; (2) dist22 > 7".0; (3) pmSigmaRa < 525 mas yr^{-1}; (4) pmSigmaDec < 525 mas yr^{-1}; (5) nFit = 6.
[d] l-color: $-0.436u + 1.129g - 0.119r - 0.574i + 0.1984$; defined for $0.5 < (g - r) < 0.8$.
[e] Reduced proper motion in the noted band: $H_{\rm band} = {\rm mag}_{\rm band} + 5 + 5\log_{10}({\rm PM}\ ({\rm arcseconds\ yr}^{-1}))$.

DR9 and later. The SEGUE-1 and SEGUE-2 target selection information in the sppTargets and segueTargetAll tables also uses the DR7 version of the recalibrated USNO-B proper motions. Comparisons of the quality and accuracy of the successive versions of the recalibrated USNO-B proper-motion catalog released with DR7, DR8, and DR9 are given in the DR9 data release paper (Ahn et al. 2012), and an overall assessment of the uncertainties is provided in Dong et al. (2011).

All of the SDSS imaging data were rereduced, and the global photometric calibration was updated in DR8 (Aihara et al. 2011; Padmanabhan et al. 2008). The DR8 version of the imaging data was the default imaging catalog for the SDSS imaging data until the DR13 release. For DR13, the imaging data were recalibrated to the Pan-STARRS 1 survey (Finkbeiner et al. 2016; Albareti et al. 2017). These changes in the photometry in turn change the values of parameters used to select stars as targets for SEGUE-2 spectroscopy. This complicates matching the most recent imaging data to the spectra, as stars that made the target section cuts using the SEGUE-2 photometry sometimes do not make the cuts with later versions of the imaging data and vice versa. This is an especially large effect in the categories that look for outliers and rare objects in the photometry and proper-motion data, for example, the M-giant category (Section 4.2.2 and Appendix A). We discuss below in Section 7 how the targeting information was included in the data releases, as well as strategies for combining the information in the imaging and spectroscopy data to create the best samples for particular types of analysis.

The SEGUE-2 photometry in the sppTargets table includes only objects classified as stars in the imaging data, and only objects classed as stars were considered as potential spectroscopic targets. All the SEGUE-2 selection criteria use magnitudes measured by fitting to the point-spread function of the data (Stoughton et al. 2002). The SDSS photometric quality flags are used to reject any object that is saturated in the imaging data. Because too much light through the fibers can cause unacceptable contamination between spectra of stars on adjacent fibers and scattered light, a bright limit of $g_{\rm fib3} > 15.5$ and $r_{\rm fib3} > 15.0$ is imposed on all targets, where fib3 is the 3″ synthesized fiber magnitudes (Stoughton et al. 2002) and is not corrected for extinction. The 3″ fiber magnitudes are 0.3 mag fainter on average than the point-spread function magnitudes. Except where explicitly specified, all magnitudes used to select spectroscopic targets in SEGUE-2 are corrected for extinction using the dust maps of Schlegel et al. (1998) so that the sample depth is approximately independent of the foreground extinction. Thus, we omit the usual subscript that indicates that a magnitude has been corrected for extinction when discussing targeting.

The target selection categories for the SEGUE-2 survey are summarized in Table 1. The target classes are shown in color–apparent-magnitude space in Figure 2 and in color–color space in Figure 3. Each class is described in more detail below.

4.1. Blue Horizontal-branch Candidates

BHB stars are powerful tracers of the halo because they are usually produced by an old, metal-poor population and have a narrow range of absolute visual magnitudes, increasing the precision of distance determinations (e.g., Xue et al. 2008; Santucci et al. 2015a). The SEGUE-2 BHB category selects stars bluer than the main-sequence turnoff but not as blue as white dwarfs: $-0.5 < g - r < 0.1,\ 0.8 < u - g < 1.5$. This selection contains true BHB stars with low surface gravity as well as higher surface gravity A-colored objects, which we refer to here as "blue stragglers" (BS) or "A main-sequence" objects. We note that for surveys with no u band available, BHB and BS stars may be effectively separated using sufficiently deep z-band observations in combination with g- and either r- or i-band observations (Vickers et al. 2012; Whitten et al. 2019).

The limiting magnitude for this category was $g = 20.3$. Objects that pass the color criteria with $g < 19.5$ have higher priority than objects with $19.5 < g < 20$, which in turn have
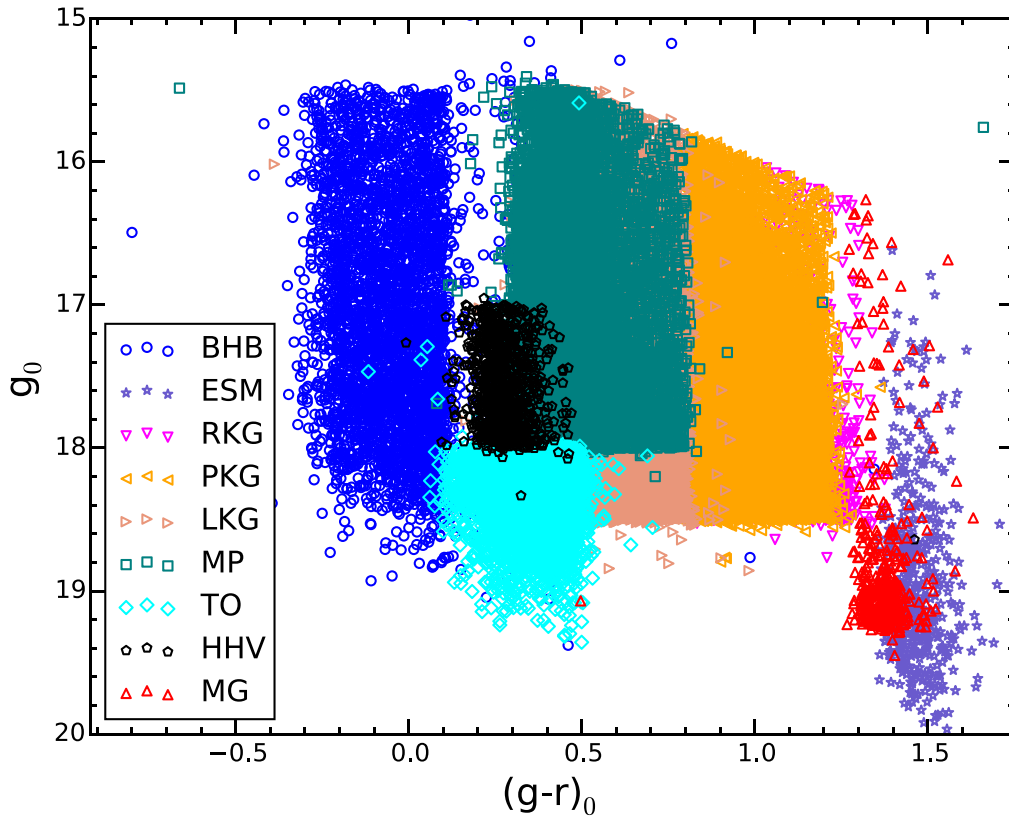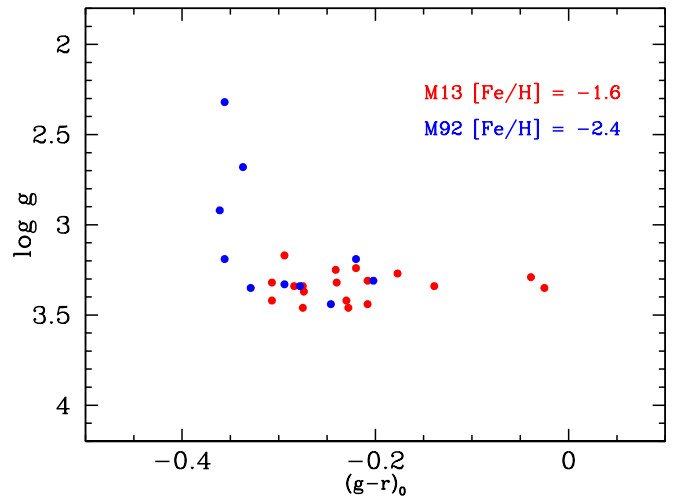
Figure 2. Color–magnitude diagram for the SEGUE-2 sample with major target classes indicated. BHB stands for blue horizontal-branch stars, ESM extremely cool subdwarfs, TO main-sequence turnoff stars, RKG red K giants, LKG *l*-color K giants, PKG proper-motion K giants, MP low-metallicity targets, HHV high-velocity halo stars, and MG M giants.
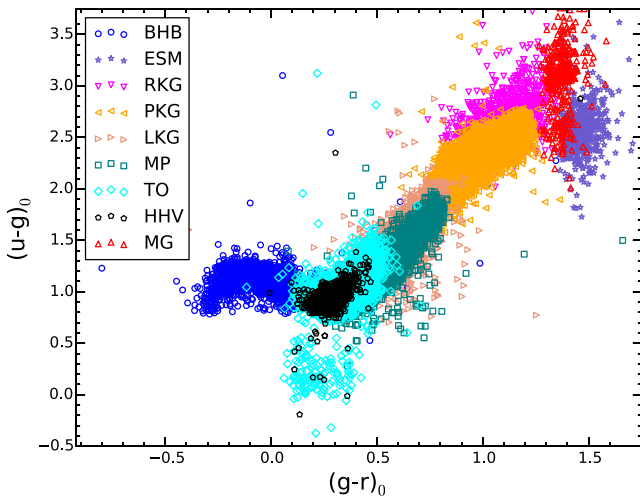
Figure 3. Color–color diagram for the SEGUE-2 sample with major target classes indicated, as described in Figure 2.

Figure 4. SSPP log g values for spectroscopically verified BHBs that are confirmed members in clusters M13 and M92. It can be seen that most BHB stars have SSPP log g values between 3.1 and 3.5, but that the hottest BHB stars in M92 have lower values, ranging up to 2.3. All of these stars have spectra with S/N > 35.

higher priority than objects with $20 < g < 20.3$. The priorities are used to ensure that all the brighter stars in the footprint are observed because their spectra yield the most accurate velocity and parameter measurements.

The SSPP uses the method of Wilhelm et al. (1999) to combine *ugr* colors and the Balmer line profiles ($D_{0.2}$) to estimate $T_{\rm eff}$, log g, and [Fe/H] for these hot BHB candidates. To isolate a sample of BHB stars from BS or A main-sequence stars, cuts in stellar parameters are required. To investigate the reliability of the parameters for BHB stars, SEGUE-1 targeted

them in two clusters: M13 and M92. We identified genuine members of the clusters using a combination of RV, proper motion, and position on the color–magnitude diagram (CMD) (full details are given in Morrison et al. 2016). We show in Figure 4 that these confirmed BHB members of the globular clusters have SSPP log g ranging from 2.3 to 3.5, with only the bluest stars in the very-metal-poor cluster M92 having log g less than 3.0.

Yanny et al. (2009), Harrigan et al. (2010), Deason et al. (2010, 2011), and Fermani & Schönrich (2013) all used cuts in $\log g$, $T_{\rm eff}$, and ugr to identify purer BHB samples to study the halo's kinematics and density distribution. Deason et al. (2011) used a $\log g$ range from 2 to 4, while Fermani & Schönrich (2013) suggested a narrower range of $\log g = 2$–3.3, the latter being more conservative than the results in Figure 4 suggest.

In addition, some investigators have used reanalysis of the SEGUE spectra to reduce contamination by gaining more information. Sirko et al. (2004b) fit the Balmer line profiles, following Clewley et al. (2002). Adopting this technique can reduce the contamination rate to significantly less than 10%, allowing Xue et al. (2008) to measure the mass of the Milky Way out to 60 kpc, and Ruhland et al. (2011) and Kafle et al. (2012) to study halo streams. Santucci et al. (2015b) added another criterion to the Clewley et al. technique, basing their additional method on the depth and width of Balmer lines, first used by Pier (1983). Santucci et al. (2015a) then use the BHB sample to map the halo's age distribution.

A total of 9744 unique objects in this category were targeted for SEGUE-2. Matched to the DR8 photometry, which is not identical to the targeting photometry, 9660 candidates in this category have DR8 photometry available. Of these 9660 objects with matched DR8 photometry, 7327 have a valid (non –9999) measurement for the parameter LOGGADOP.

4.2. Luminous Red-giant Stars

Red giants are the most-luminous tracers available in old populations and so are a particularly important target category for the study of the distant halo. Depending on the metallicity, the tip of the giant branch of an old population falls either in the K-giant region (for metal-poor stars) or the M-giant region (for metal-richer stars). SEGUE-2 used different target selection criteria for K and M giants, described separately below.

4.2.1. K Giants

The most-luminous metal-poor K giants have $M_g \sim -2$, which means that even a star as bright as $g = 18.5$ can be seen to 120 kpc, making these stars the tracers of choice for in situ studies of the outer halo. Unfortunately, at these magnitudes, nearby K dwarfs vastly outnumber distant K giants. SEGUE-2 used three different criteria to separate K giants from K dwarfs.

The three K-giant categories are shown in color–color space in Figure 5. The giant locus in the $u - g$, $g - r$ diagram is affected both by luminosity and metallicity. Giants are found below the locus of foreground dwarfs for the bluer part of the K-giant range, cross the locus near $g - r = 0.8$, and are found above the locus for redder colors.

The rarest targets (at the tip of the giant branch) belong to the red K-giant category, with fewer than 20 per 7 deg² plate, except on the lines of sight with the highest stellar density. All stars that passed the red K-giant target criteria were observed (unless blocked by fiber collisions). Within the l-color K-giant region (the l-color is defined in Lenz et al. 1998; see footnote to Table 1), stars with $g - r$ greater than 0.6 were given priority over the bluer stars because the redder giants are more luminous. Unfortunately, there is no way to use ugr to favor the selection of high-luminosity, low-metallicity K giants in the proper-motion K-giant region, but as the name implies, it is still possible to achieve reasonable efficiency for targeting giants in this region with a proper-motion cut to reject foreground
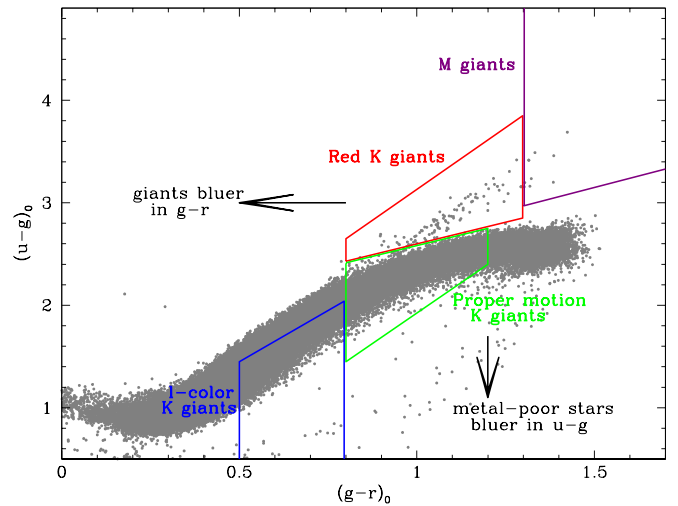
Figure 5. $u - g$ vs. $g - r$ diagram illustrating the K- and M-giant target types for SEGUE-2. Gray points are stars from the Stripe 82 catalog of Ivezić et al. (2007), which have particularly accurate photometry. The red K giants occupy the region where K giants are found above the locus (of predominantly foreground dwarfs), the proper-motion K giants sample this locus at the red end of the K-giant color range, and the l-color K giants occupy the region where metal-poor stars are found below the locus. The M giants form the continuation to the red of the red K-giant sequence.

dwarfs. The limit used was total proper motion <11 mas yr^{-1}, which is a 2σ limit for the SDSS proper motions (see the discussion of the recalibrated USNO-B proper motions earlier in this section). Stars in the proper-motion K-giant region were assigned to fibers until the total number of K-giant targets was 150 per 7 deg² plate. If other SEGUE-2 target categories did not have enough stars to meet their fiber quotas, which happened at very high latitudes, the extra fibers were assigned to this category.

Each of the three target types imposes different metallicity biases. The l-color sample is only complete below [Fe/H] $= -1.5$. The red K giants include the most metal-rich stars in the SEGUE-2 K-giant sample because the metal-rich red-giant branch stands out more from the stellar locus and the luminosity separation is largest for metal-rich giants. The targeting of K giants using the $u - g$ versus $g - r$ diagram is discussed in more detail in Yanny et al. (2009). While the combination of the red K-giant and the proper-motion K-giant classes can be used to produce a relatively unbiased sample of the K-giant metallicity distribution, it should be remembered that the actual numbers of stars observed in each category are quite different, and so it is necessary to correct for sampling biases following either the weighting method of Schlesinger et al. (2012) or a Bayesian formalism such as that used by Xue et al. (2015).

The probability of actually observing a K giant is a strong function of magnitude and color. The number of foreground dwarfs increases toward redder colors and fainter magnitudes and in fields that are at lower Galactic latitudes and Galactic longitudes far from the anticenter. In addition, the halo is very centrally concentrated (e.g., Vivas & Zinn 2006; Xue et al. 2015), so the redder, fainter stars that belong to the outer halo are very rare. Therefore, selection efficiency ranges from a few percent for the reddest stars near the faint magnitude limit of our selection at $g < 18.5$ to greater than 50% for the brightest stars in the red K-giant region ($g < 17$), which stand out best

Table 2
Codes for `FLAG`

Position	Flag	Description	Category	Parameters
First	n	Appears normal		Yes
	D	Likely white dwarf	Critical	No
	d	Likely sdO or sdB	Critical	No
	H	Hot star with $T_{eff} > 10,000$ K	Critical	No
	h	Helium line detected, possibly very hot star	Critical	No
	l	Likely late-type solar-abundance star	Cautionary	Yes
	E	Emission lines in the spectrum	Critical	No
	S	Sky spectrum	Critical	No
	V	No radial velocity information	Critical	No
	N	Very noisy spectrum	Cautionary	Yes
Second	n	Appears normal		Yes
	C	The photometric $g - r$ color may be incorrect	Cautionary	Yes
Third	n	Appears normal		Yes
	B	Unexpected Hα strength predicted from Hδ	Cautionary	Yes
	b	If d or D flag is not raised among stars with B flag		Yes
Fourth	n	Appears normal		Yes
	G	Strong G-band feature	Cautionary	Yes
	g	Mild G-band feature	Cautionary	Yes
Fifth	n	Appears normal		Yes
	B	Too blue $(g - r)_0 < -0.3$ to estimate parameters	Critical	No
	R	Too red $(g - r)_0 > 1.3$ to estimate parameters	Critical	No
	X	No parameter estimate	Critical	No
	c	Correlation coefficient < 0.4	Cautionary	Yes
	T	Difference between adopted T_{eff} and IRFM $T_{eff} > 500$ K	Cautionary	Yes
	P	Predicted $g - r$ may be wrong	Cautionary	Yes

from the rest of the stellar locus and have the most accurate photometry, especially in the u band.

H. L. Morrison et al. (2022, in preparation) describe the construction of a clean sample of SEGUE K giants using the SSPP measures of $\log g$ and [Fe/H] and an additional spectroscopic luminosity indicator based on the Mgb/MgH feature near 5170 Å, and several "sanity checks" to remove erroneous data because halo K giants are rare compared to foreground disk dwarfs. This sample contains ~15,000 spectroscopically confirmed K giants, an enormous increase in size from previous samples. We note that carbon-enhanced metal-poor (CEMP) K giants were eliminated from this sample using the SSPP "strong G-band feature" flag (see Table 2). Thus, the final sample described in Morrison et al. contains relatively fewer CEMP K giants than are present in reality. These CEMP K giants will be presented in T. C. Beers et al. (2022, in preparation).

Xue et al. (2014) published both the spectroscopic parameters for 6036 giants and their distances, calculated using a Bayesian scheme that accounts for biases caused by the giant-branch luminosity function. They chose to calculate distances only for giants more luminous than the horizontal branch to avoid confusion between first-ascent giants and red horizontal branch stars. This accounts for the reduction in the size of the sample from around 15,000 to 6036 because the lower giant branch is more heavily populated than its upper regions.

Janesh et al. (2016) and Xue et al. (2015) use the Morrison et al. sample described above to quantify the amount of substructure in the halo and to measure its density distribution and its metallicity gradient, finding a weak gradient (a drop of 0.11 dex from 10 to 65 kpc), which they point out will likely become weaker when the metallicity selection effects of the l-color K-giant category are taken into account. The omission of

the CEMP giants from their sample will affect the number of extremely iron-poor K giants measured. Work to model the in situ halo metallicity gradient using all three K-giant target types (the red K-giant and proper-motion K-giant categories are particularly important for the metal-richer portion of the halo) is currently underway.

Yang et al. (2019) identify a sample of over 13,000 K giants from the LAMOST survey, implementing a very similar procedure to that used to identify SEGUE K giants. They identify halo substructure and show, in agreement with Janesh et al. (2016), that the amount of substructure increases with distance and metallicity. Further work with this sample has provided new limits on the mass of the dark halo (Zhai et al. 2018) and the velocity anisotropy of the stellar halo (Bird et al. 2019).

4.2.2. M Giants

Metal-rich stars, such as the most metal-rich stars in the Sagittarius stellar populations, become M giants at the end of their lives. Therefore, M giants are a ready tracer of massive, late accretion events (e.g., Majewski 1993). For example, this spectral type is common in the M31 halo (e.g., Gilbert et al. 2006). The M-giant category was designed to identify the reddest stars in the halo to investigate the contribution of metal-rich stars to the halo of the Milky Way. Unfortunately for this goal, the largest population at red colors and faint magnitudes in the Milky Way is M dwarfs. Therefore, it is crucial to distinguish giants from dwarfs photometrically. The two-color plot in $u - g$, $g - r$ that was used to target red K giants shows that the separation in these colors extends to colors with $g - r > 1.3$. Therefore, the selection criteria for M-giant candidates is $g - r > 1.3$, $u - g > 1.8 + 0.9(g - r)$. This is similar in spirit to the near-infrared photometric method used by Majewski et al. (2004), for example. To further reduce

contamination by foreground dwarfs, the measured proper motion must be at least 2σ away from a total proper motion of 11 mas yr^{-1}. All candidates were required to have good proper-motion measurements. To reduce contamination by spurious outliers from the much more common dwarf population at similar $g - r$ colors, the errors in g and r point-spread function (psf) magnitudes for all candidates were required to be <0.05 mag. The targets were limited to $i > 14.5$ as an additional precaution against scattered light. The magnitude range $15.5 < g < 19.25$ was set to ensure sufficiently high S/N to measure reliable gravity indicators in the spectra.

While this category could receive up to 50 fibers, there were few stars in most SEGUE fields matching these criteria. As a result, almost every candidate received a fiber, making SEGUE the most complete survey for faint M giants in the halo. The deep molecular bands in the spectra of M stars make them difficult to model and analyze, and as a result, the stellar parameters of these stars are not determined by the SSPP. Spectral indices, however, are correlated with M-star properties and can be used to evaluate stellar properties (Schiavon & Barbuy 1999; Gilbert et al. 2006).

As preliminary tests of the number of M giants successfully detected in the halo, we used the strength of the Na I lines at 5887/5889 Å, which are much weaker in low-gravity giants than in high-gravity dwarfs (Gray 2008). Plotting the NaI20 side index from the sppLines table revealed a bimodal population separated by a wide gap. Considering all stars with an equivalent width of <5 Å as probable giants, we find that ~65 of the 569 targeted stars would qualify. These low-Na stars are also characterized by smaller parallaxes from Gaia DR2 and larger radial velocities than those of the high-Na targets.

These M-giant candidates were then inspected by eye, using the weakness of the Na I lines at 5890, 5896 Å and 8183, 8195 Å; the Ca I lines at 6103, 6122, and 6162 Å; and the K I lines at 7665, 7699 Å (Turnshek et al. 1985) to check their luminosity. We found that only 18 were in fact M giants, 2 were classical C stars, and the remainder were K giants, some of which were quite metal poor. Therefore, we estimate the success rate of the M-giant selection as ~5%, reflecting the small number of M giants in the halo.

To further illustrate the overlap between the K- and M-giant categories, we searched the SDSS database for stars with $(g - r)_0$ greater than 1.2 and values of the Na I index lower than 5. Figure 6 shows that there is a significant overlap in both directions between the K and M giants, which is to be expected when a photometric cut is used to separate different spectral types. It also shows that the classical carbon stars occupy a different region in the $u - g$, $g - r$ plane.

4.3. Candidate Metal-poor Stars

The metal-poor star category in SEGUE-2 selected targets on the basis of colors and apparent magnitudes (see Table 1; these cuts are similar, though not identical, to those used for metal-poor targets in SEGUE-1).

Based on SSPP estimates of metallicity, the number of known very/extremely metal-poor stars ([Fe/H] < −2 and [Fe/H] < −3, respectively) has been expanded 10 fold: SDSS Legacy (5970 very-metal-poor/203 extremely metal-poor stars), SEGUE-1 (12,598/331 stars), and SEGUE-2 (7670/208 stars), for a total of over 26,000 stars with [Fe/H] < −2 dex, counting only stars with $4500\,K < T_{eff} \leqslant 7500\,K$. The
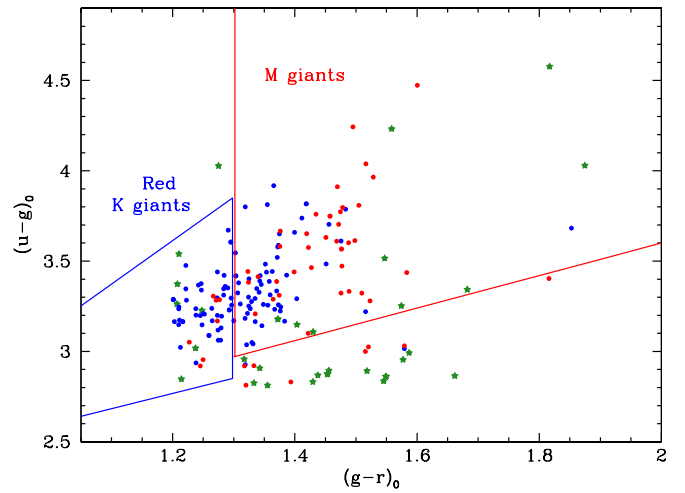
Figure 6. $(u - g)_0$ vs. $(g - r)_0$ diagram illustrating the overlap between K and M giants in their respective target types. Spectroscopically confirmed K giants are shown with blue symbols, M giants with red, and carbon stars as green stars.

SSPP is well calibrated down to [Fe/H] ~ −4.0. However, for stars with [Fe/H] < −3.0, there are two effects that can perturb estimates of metallicity: (1) the presence of significant interstellar absorption in the region of the Ca II K line, and (2) potential contamination of the Ca II K line by molecular CH features, because many extremely metal-poor stars have enhanced carbon abundances (e.g., Beers & Christlieb 2005; Lee et al. 2013). Intermediate- or high-resolution follow-up observations are therefore needed to confirm extremely metal-poor candidates. Dedicated searches for the most metal-poor stars (e.g., Aoki et al. 2012; Caffau et al. 2013) are well underway, and to date, SDSS I–IV candidates account for 7 of the 14 stars known with [Fe/H] < −4.5.

High-resolution spectroscopic follow-up of SDSS/SEGUE stars has been used to examine the nature of carbon-enhanced metal-poor stars in the halo system of the Galaxy (e.g., Bonifacio et al. 2015; Yoon et al. 2016), the binary fractions of very-metal-poor stars (Aoki et al. 2015), the discovery of the first example of a main-sequence star with enhanced r-process elements (Aoki et al. 2010), and the first star with the distinctive abundance pattern associated with the explosion of a very massive ($M > 100\,M_\odot$) star in the early universe (Aoki et al. 2014).

4.4. Color-selected Main-sequence Turnoff Stars

Newberg et al. (2002) showed that main-sequence turnoff (MSTO) stars could be used to trace substructure in the halo because in the halo's generally old and metal-poor population, the turnoff is a well-defined feature distinctly bluer than the colors of red giants and dwarfs from the disk. These MSTO stars are considerably more numerous, though less luminous, than the BHB and K-giant stars and therefore complement them as halo tracers. By obtaining spectra of MSTO stars in the SEGUE-2 fields, we aimed to provide radial velocities and metallicities for this valuable population.

The color limits of this category are set to include stars at the MSTO for old populations with [Fe/H] ⩽ 0. The blue limit at $g - r > 0.1$ is set to be the same as the red edge of the BHB selection. The red limit at $g - r < 0.48$ is set at the MSTO color of a 10 Gyr old solar-metallicity population (Bressan et al.

2012). More metal-poor stars of the same age or younger will have bluer colors, while slightly younger populations of more metal-rich stars, such as the turnoff of NGC 6791, will also fall within the color boundaries. The age–metallicity relations found for populations such as the Sagittarius dSph show that more metal-rich populations are younger than 10 Gyr (e.g., Siegel et al. 2007). Given that, the red limit is a generous compromise between a sample unbiased in metallicity and the increased volume sampled by including only the most luminous part of the main sequence. The red limit also avoids repeating the SEGUE G-dwarf sample for which the fiber allocation, and therefore sampling density per line of sight, is much larger than allocated for the MSTO selection in SEGUE-2. We note that, while SEGUE-1's F-star target selection only included objects with $0.4 < u - g < 1.4$, there was no $u - g$ color cut applied in SEGUE-2. This makes the SEGUE-2 selection less biased toward low metallicity, but objects with hot, flat spectra, mostly quasars, with $u - g < 0.4$, remain in the sample (see Figure 3).

The absolute magnitude range that falls within those color cuts for old populations is about $4 < M_r < 6$ (Bressan et al. 2012). The faint magnitude limit is set so that all spectra in this category have sufficient S/N for the determination of metallicity estimates from the SSPP. The bright limit is set such that the sample is dominated by the halo. For a magnitude range of $18 < r < 19.5$ and $M_r = 4$, the distance shell sampled is 6.3 kpc to 15.8 kpc. For $M_r = 6$, the distance range is 2.5–6.3 kpc. Belokurov et al. (2014) used these stars as well as BHB stars and M giants to trace the tidal debris of Sagittarius.

4.5. High-proper-motion-selected M Stars

This category selects for relatively nearby, cool stars with apparent large transverse motions and colors consistent with a metal-poor atmosphere. Such stars are hypothesized to be low-mass, main-sequence members of the Galactic old disk or halo, the so-called "M subdwarfs" or "sdM" stars (Gizis 1997; Lepine et al. 2007). To identify nearby stars with large transverse motions, we use a selection based on the reduced proper motion $H_g \equiv g + \log \mu + 5$, where μ is the measured proper motion. We avoid the selection of the faintest targets, whose proper motions may not be well measured. Contamination from field M dwarfs with large transverse velocities is still expected. The criterion in color–color space selects most known sdM stars in the vicinity of the Sun, while excluding the majority of field M dwarfs; this is because low-mass, metal-poor stars have significantly redder $g - r$ colors and bluer $r - i$ colors as a function of effective temperature, due to reduced molecular band opacities in the r band (Lépine & Scholz 2008).

A total of 9213 stars fall into this category. In addition, these objects were complemented by the manual selection of a number of high-proper-motion stars identified in the SUPERBLINK (Lépine et al. 2002) proper-motion survey, which, at the time of selection, did not have measured proper motions in the SDSS source catalog. Those targets were included as they were identified in the SUPERBLINK survey and included in the MAN category. They were selected using the same criteria as above, but with the μ value taken from the SUPERBLINK proper-motion survey. Some 1128 additional targets were thus selected.

4.6. Candidate High-velocity Halo Main-sequence Turnoff Stars

The kinematic properties of the highest velocity stars in the halo are shaped by dynamic processes such as tidal shocking, heating, and stripping during the accretion and merging events that formed the Milky Way halo. The goal of this selection is to create a sample of very high-velocity stars in the halo beyond the solar neighborhood. The selection targets stars with total 3D velocities >300 km s^{-1}, as estimated from their proper motions, measured to an accuracy greater than 3σ. The selection criteria are

$$17 < g < 19.5$$
$$0.1 < g - r < 0.48$$
$$\widetilde{V}_{\rm perp} > 300 \text{ km s}^{-1}$$
$$\frac{\widetilde{V}_{\rm perp}}{\widetilde{\sigma}_{V\,\rm perp}} > 3.$$

The shape of the Munn et al. (2004) proper-motion error distribution is analyzed in more detail in Dong et al. (2011), and the proper-motion errors are also evaluated in Vickers et al. (2015). The selection also imposes the basic proper-motion quality cuts for the Munn et al. (2004) catalog recommended by Kilic et al. (2006).

The stars are drawn from a color and magnitude selection similar to the main SEGUE-2 main-sequence turnoff sample (Section 4.4): $17 < g < 19.5$, $0.1 < g - r < 0.48$. This extends brighter by about a magnitude to take advantage of the more accurate proper motions at brighter magnitudes because the high-velocity selection should remove disk stars that would otherwise overwhelm the sample. The photometric parallax relation

$$M_g = 5.7 + 10(g - r - 0.375)$$

is used to estimate an approximate distance modulus and distance d_{Mg} for each star. The M_g estimate has an uncertainty of about 0.2 mag, as estimated from the M3, M13, and M5 data in the SDSS filters from An et al. (2008).

The 3D velocity vector in Cartesian coordinates for each star is then estimated as

$$\widetilde{V}_{\rm perp} = 4.74 d_{Mg}(-\mu_\alpha \sin({\rm R.A.}) - \mu_\delta \cos({\rm R.A.})\sin({\rm decl.}),$$
$$\mu_\alpha \cos({\rm R.A.}) - \mu_\delta \sin({\rm R.A.})\sin({\rm decl.}), \mu_\delta \cos({\rm decl.}))$$
$$+ V_\odot - r(r \cdot V_\odot),$$

where $V_\odot = (108.1, -112.5, 172.2)$ km s^{-1} is the Sun's velocity vector with respect to the GC in Cartesian coordinates, and r is the position vector to the star. The estimated tangential velocity $\widetilde{V}_{\rm perp}$ is the magnitude of that vector. The uncertainty in $\widetilde{V}_{\rm perp}$ is

$$\widetilde{\sigma}_{V\,\rm perp} = 4.74 d_{Mg} \sigma_{\rm PM}.$$

The value of $\sigma_{\rm PM}$ is estimated as in Dong et al. (2011) but for r as

$$\sqrt{4.56^2 + f_r 2.3^2}$$
$$f_r = 10^{0.4(r-19.5)}.$$

The selection requires that the estimate of the 3D velocity $\widetilde{V}_{\rm perp}$ (not the proper motion) be greater than 3σ: $\widetilde{V}_{\rm perp}/\widetilde{\sigma}_{V\,\rm perp} > 3$.

A total of 4297 objects fall into this category.

4.7. Candidate Old-population Hypervelocity Stars

SEGUE-2 targeted a sample of stars whose colors and kinematics indicated a potential expulsion from the GC—the HVS. This experiment, designed to locate the "metal-rich contaminant" to the Galactic halo originally envisioned by Hills (1988), selects stars with a high probability of being high metallicity and with proper motions consistent with high space velocities from the GC.

We chose stars with a perceptible proper motion from the USNO-B proper-motion measurements (total proper motion $\mu > 8$ mas yr^{-1}) and a total space velocity $v_{tot} > 400$ km s^{-1}. In addition, we require either (a) the tangential velocity $v_{tang} > 400$ km s^{-1} or (b) the component of proper motion in the direction perpendicular to the line joining the star to the GC $\mu_{\perp} < 6$ mas yr^{-1}. This latter requirement is intended to remove stars with a large velocity that are not ejected from the GC. Lastly, we require $u - g$ and $g - r$ colors designed to select old metal-rich stars. The details of the target selection can be found in Table 1. These criteria are applied in addition to those applied to all SEGUE-2 targets involving proper motions that remove poorly measured objects due to errors in USNO-B. The selection described above resulted in a total of 361 target stars within 181 SEGUE-2 fields. For more details about the selection criteria we refer the reader to Kollmeier et al. (2010). In addition, Kollmeier et al. (2009) report on the detection of six very interesting metal-poor HVS candidates but find no metal-rich HVS objects. The metal-poor HVS candidates provided one of the first hints of a truly low-metallicity population in the GC. Most importantly, the rigorous selection allowed for tight constraints on the high-metallicity mass function at the GC, combined with the ejection mechanism of HVS generally.

5. SEGUE Stellar Parameter Pipeline Update

The SEGUE Stellar Parameter Pipeline (SSPP) (Lee et al. 2008a; Smolinski et al. 2011) determines atmospheric parameters T_{eff}, log g, and [Fe/H] from SDSS/SEGUE stellar spectra of both giants and dwarfs spanning more than three orders of magnitude in metal content and 6000 K in effective temperature. The SSPP prioritizes consistent measurements for stellar parameters across this broad range of temperature, metallicity, and gravity. As a result, SDSS/SEGUE data can be used to study the nearby and distant Galaxy using stars with different T_{eff} and luminosity to span as large a volume of the Galaxy as possible in a magnitude-limited survey. The SSPP as originally described in Lee et al. (2008a) has been refined and modified with each new SDSS data release through DR9 to provide more accurate estimates of the stellar atmospheric parameters. In this paper, we describe the version of the stellar parameters measured with the final SDSS version of the SSPP and made public with SDSS DR9 (Ahn et al. 2012). In Appendix B, we discuss the specific upgrades made to the SSPP between DR8 and DR9. The DR9 parameters have been carried through subsequent SDSS data releases.

The SSPP uses multiple methods to estimate stellar parameters. The parameter estimators, with the exception of the Infra-Red Flux Method (IFRM) temperature (Section 5.1), are described in detail in Lee et al. (2008a). They are summarized briefly here, listed by their variable names in the SDSS public data. Some of the methods used by the SSPP find the best match between the observed spectra and a grid of

Table 3
Summary of Methods Used in the SSPP

Method	$(g - r)_0$	S/N	Wavelength Range (Å)	T_{eff} (K)	log g (cgs)	[Fe/H]
ki13	0.0–0.6	⩾20	4400–5500	✓	✓	✓
k24	0.0–0.6	⩾15	4400–5500	✓	✓	✓
WBG	−0.3–0.3	⩾10	3900–6000	✓	✓	✓
ANNSR	−0.3–0.7	⩽15	3850–9000	✓	✓	✓
ANNRR	−0.3–1.2	⩽10	3850–9000	✓	✓	✓
NGS1	−0.3–1.3	⩾10	4500–5500	✓	✓	✓
HA24	0.1–0.8	⩾10	∼6563	✓		
HD24	0.1–0.6	⩾10	∼4102	✓		
NGS2	0.0–1.3	⩾10	4500–5500		✓	✓
Ca II	0.1–1.2	⩾15	3850–4250		✓	✓
CaIIK2	0.1–0.7	⩾15	∼3933			✓
CaIIK3	0.1–0.7	⩾15	∼3933			✓
IRFM	−0.3–1.3	⩾10	n/a	✓		

model spectra by χ^2 minimization. Each of these methods uses the subset of wavelength range between 3850 and 6000 Å. These methods include ki13, k24, (Allende Prieto et al. 2006), WBG (Wilhelm et al. 1999), NGS1, NGS2, and CaIIK1 (Lee et al. 2008a). The ANNSR and ANNRR estimators (Fiorentin et al. 2007) employ a neural network analysis. A variety of line indices are also used to estimate parameters (e.g., Beers et al. 1999); HA24, HD24, CaIIK2, and CaIIK3 are in this category. The SSPP estimates T_{eff} via both spectroscopic and photometric methods. The spectroscopic-only estimates of T_{eff} are useful in regions of high extinction (see, e.g., Cheng et al. 2012). Photometric estimates of T_{eff} are particularly important for cooler stars for which the Balmer lines are too weak to be a useful temperature indicator at the resolution of the SDSS/SEGUE spectra. The DR9 SSPP replaces all the photometric methods used in previous versions of the pipeline with a single estimator based on the IRFM (Blackwell et al. 1980).

Each individual estimator used by the SSPP is valid for a specific range of $(g - r)_0$ and S/N (Table 3). The valid range of each estimator is specified in $(g - r)_0$ and S/N rather than T_{eff} to avoid introducing spurious features in the distribution of the derived parameters. All estimates that are valid for a particular stellar spectrum are combined to compute a final, "adopted" value for each parameter. The combination of multiple estimators allows for outlier rejection in the individual measurements and makes the final adopted parameters more robust to data reduction or other problems in the spectra and more consistent for stars over a wide range in T_{eff}, log g, [Fe/H], and S/N. The SSPP information in each data release includes the individual estimators as well as the final, adopted fundamental parameters (FEHADOP, TEFFADOP, LOGGADOP) for most stars in the temperature range 4000–10,000 K with spectral S/N > 10 per ∼1 Å pixel averaged over 4000–8000 Å.

In Section 5.1, we describe the new photometric temperatures derived for DR9 by the IRFM method. The method for combining the estimators for each parameter is described in Section 5.2. We describe the updated SSPP quality flags in Section 5.3. In Section 5.4, we present the spectra from star clusters and higher-resolution observations that provide calibration and evaluation samples for the SSPP. The calibration procedure is described in Section 5.5. In Section 6, we evaluate the performance of the DR9 SSPP using repeat observations of stars in SEGUE, star clusters, and

comparison with a set of stars reobserved at higher resolution by the APOGEE survey.

5.1. SSPP Temperature Determination from IRFM

The DR9 version of the SSPP has a significantly improved photometric $T_{\rm eff}$ estimate from the IRFM. The IRFM (Blackwell & Shallis 1977; Blackwell et al. 1980) estimates a star's effective temperature using the comparison of a star's bolometric flux with its monochromatic flux at an infrared wavelength. While stellar models are required to convert this ratio into an effective temperature, the result is not strongly dependent on the model used (e.g., Asplund & García Pérez 2001). L. Casagrande (2012, private communication) has directly determined IRFM $T_{\rm eff}$ values for some 13,000 SDSS/SEGUE stars with good 2MASS JHK_s photometry, clean $ugriz$ photometry, low reddening, SDSS/SEGUE spectra, and good SSPP estimates of $\log g$ and [Fe/H]. In addition, the spectra were checked by eye by one of us (T.C.B.) to remove outliers in SSPP estimates. The procedure followed the IRFM technique as implemented by Casagrande et al. (2006, 2010). The IRFM technique uses all photometric passbands to estimate the bolometric flux, and each of the IR passbands produces a separate estimate of $T_{\rm eff}$. In addition, IRFM temperatures were derived for the SDSS/SEGUE stars reobserved at higher resolution (Section 5.4) that had 2MASS photometry available. In this case, the high-resolution values of $\log g$ and [Fe/H] were used in the IRFM estimation procedure.

Casagrande used these data to derive two polynomial relationships (one for giants and one for dwarfs) that use a star's $g - i$ color and its [Fe/H] to estimate its $T_{\rm eff}$. Similar color−temperature relationships have already been derived for colors in other photometric systems (e.g., Alonso et al. 1996; Ramírez & Meléndez 2004; Casagrande et al. 2010). Such color−temperature relations make it possible to estimate $T_{\rm eff}$ without using the full IRFM methodology and to do so for stars that are too faint to have accurate JHK_s values in 2MASS.

The adopted relation used by the DR9 SSPP for obtaining the IRFM temperature from $g - i$ color, [Fe/H], and $\log g$ is

$$T_{\rm eff,IRFM} = 5040/(a0 + a1 \cdot X + a2 \cdot X^2 + a3 \cdot X^3$$
$$+ \, a4 \cdot X \cdot [{\rm Fe/H}] + a5 \cdot [{\rm Fe/H}] + a6 \cdot [{\rm Fe/H}]^2), \quad (1)$$

where X is $(g - i)_0$ and (i) for dwarfs ($\log g \geqslant 3.7$) $a0 = 0.6787$, $a1 = 0.3116$, $a2 = 0.0573$, $a3 = -0.0406$, $a4 = -0.0163$, $a5 = -0.0021$, and $a6 = -0.0003$; (ii) while for giants ($\log g < 3.7$) $a0 = 0.6919$, $a1 = 0.3091$, $a2 = 0.0688$, $a3 = -0.0428$, $a4 = -0.0078$, $a5 = -0.0086$, and $a6 = -0.0042$.

Because the IRFM relation depends on the metallicity and surface gravity of the stars in question, an iterative procedure is used for the SSPP IRFM $T_{\rm eff}$ estimate. The metallicity and gravity determined by NGS1 are used in this equation to obtain the first guess for $T_{\rm eff}$. With this first-pass estimate of $T_{\rm eff}$ held fixed, χ^2 minimization in the NGS1 synthetic spectra grid is used to obtain a new estimate of $\log g$ and [Fe/H]. These new values of $\log g$ and [Fe/H] are used in a second iteration in Equation (1) to determine the final SSPP estimate of $T_{\rm eff}$ from IRFM.

In Figure 7 we compare $T_{\rm eff}$ from the full implementation of the IRFM with both the SSPP spectroscopic $T_{\rm eff}$ (top two panels; the SSPP spectroscopic $T_{\rm eff}$ is obtained from averaging the spectroscopic methods listed in Table 3) and the SSPP
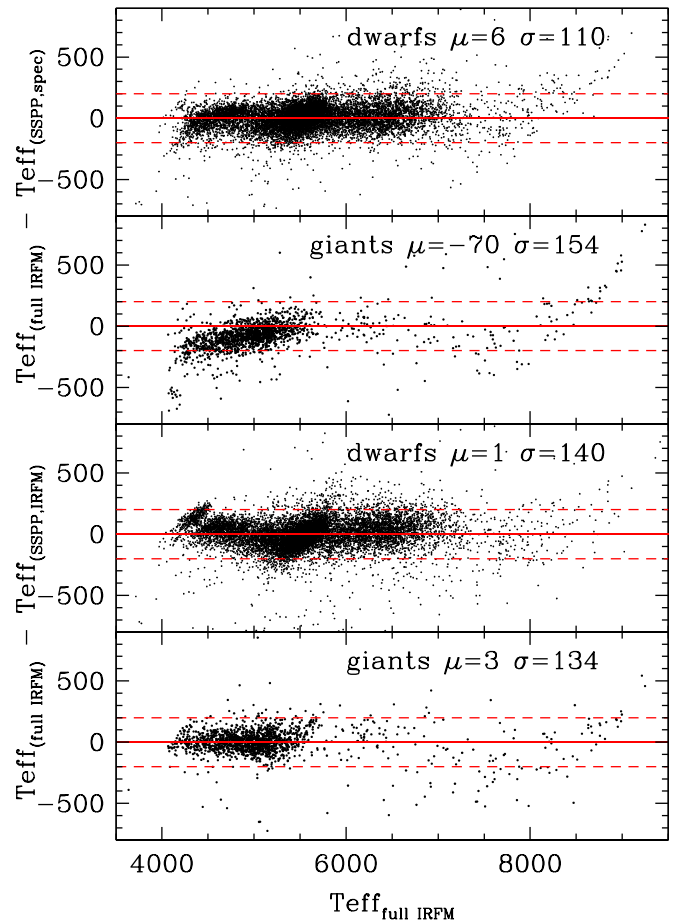
Figure 7. Comparison of spectroscopic (top two panels) and IRFM $T_{\rm eff}$ (bottom two panels) from the SSPP with the fundamental IRFM $T_{\rm eff}$ calculated using both SDSS photometry and 2MASS data. Comparisons are shown for both dwarfs and giants, separated at $\log g = 3.5$. The SSPP spectroscopic $T_{\rm eff}$ works well for dwarfs but diverges from the 1:1 line by more than 200 K for giants. The SSPP IRFM temperature shows no such systematic trend and so is recommended for giant stars.

implementation of the IRFM described above (bottom two panels). It can be seen that for dwarf stars ($\log g \geqslant 3.5$), there is good agreement with the IRFM for both SSPP methods. The zero points of the differences are close to zero, and the sigma of the differences are 110 K for the SSPP spectroscopic $T_{\rm eff}$ and 140 K for the SSPP IRFM $T_{\rm eff}$. The IRFM temperatures have a typical error between 70 and 100 K (Casagrande et al. 2006), so this implies that for dwarf stars, the errors on the SSPP spectroscopic temperatures are of order 70 K and the SSPP IRFM temperatures have errors of order 110 K.

For giants, the situation is different. We see a strong trend for the SSPP spectroscopic temperatures, with a mean of –70 K and a sigma of 154 K. The SSPP IRFM temperatures behave much better, with a mean difference near zero and a sigma of 134 K. This implies an error on the SSPP IRFM temperatures of giants of around 100 K.

Thus, we recommend that for giants, neither the SSPP TEFFADOP nor the SSPP TEFFSPEC be used. Instead, the SSPP TEFFIRFM is our recommended method. Note that the final SSPP TEFFADOP for all stars is an average of all methods but is dominated by the spectroscopic methods.

If either the g band or i band is saturated, then TEFFIRFM will be inaccurate, although there will still be a value reported. This can be avoided by checking for the saturation flag in the

photometric data if using SSPP IRFM parameters for bright stars. It is also important to remember that while the extinction-corrected colors were used to compute TEFFIRFM, a change of reddening by ± 0.01 mag will shift the IRFM $T_{\rm eff}$ by roughly ± 50 K.

We also see an offset between SSPP and full IRFM temperatures hotter than 8000 K. However, because the IRFM is only calibrated against fundamental observations (interferometry) of stars cooler than 7000 K, it is difficult to reach strong conclusions for these hot stars.

5.2. Combining Estimates from Different Methods

The SSPP uses multiple methods (NGS1, WBG, etc., described briefly in the introduction to this Section) to obtain estimates of the atmospheric parameters for stellar spectra over a very wide range in parameter space. Each individual method estimates the three stellar parameters $T_{\rm eff}$, log g, and [Fe/H] self-consistently, with calibration corrections applied as described in Section 5.5. To compute a final, "adopted" value for each of the three stellar atmospheric parameters, the SSPP takes a robust average of the individual estimates of each parameter. Because each method works over a limited range of the data, defined in the SSPP as limits in S/N and $(g - r)_0$ color (see Table 3), it is necessary to specify which methods were included in the estimation of the final, adopted atmospheric parameters for each spectrum. These are named FEHADOP, TEFFADOP, and LOGGADOP in the SDSS database and data model. This information is recorded in an indicator variable associated with each of the methods the SSPP uses to estimate the parameters of each spectrum. For example, the [Fe/H] estimate for a stellar spectrum from the NGS1 method has indicator variable FEHNGS1IND, the $T_{\rm eff}$ estimate from the ANNSR method has indicator variable TEFFANNSRIND, and similarly for all the estimators in the SSPP. The value of an indicator variable can be 0, meaning the parameter estimate is dropped because it is outside the $(g - r)_0$ or S/N limits in Table 3, (1) meaning the parameter estimate is within the limits for this spectrum and included in the final average or (2) is used in the case of [Fe/H] (see below). It is recommended that the SSPP adopted $T_{\rm eff}$, log g, and [Fe/H] calculated by these decision trees are used: TEFFADOP, LOGGADOP, and FEHADOP, respectively. In a few cases, in specific, limited parts of parameter space, a single estimate may be more accurate than the adopted average, as with TEFFIRFM for giants, as described in Section 5.1.

The exact names of the variables that hold the parameter estimates from each method, as well as the indicator and flag variables described here and below, can be found in the data model that describes the sppParams table in the SDSS data releases. The names of the parameters are descriptive of the methods used to derive them, as listed in the introduction to this section (e.g., NGS1, ANNSR, etc.). We describe in more detail how the SSPP averages estimates from multiple methods to compute each of TEFFADOP, LOGGADOP, and FEHADOP below.

There are nine temperature estimates determined by the DR9 SSPP, including the new IRFM estimate. Averages are taken of these nine estimators using the robust biweight procedure. There is also an averaged spectroscopic temperature estimate based on the methods that do not use any color information: ki13, ANNSR, ANNRR, NGS1, HA24, and HD24. A robust average of the temperature estimates with indicator variables

equal to 1 is taken for the final adopted temperature, named TEFFADOP, and the spectroscopic-only temperature, named TEFFSPEC. An estimate of the scatter around the average value is measured for both TEFFADOP and TEFFSPEC, and recorded as TEFFADOPUNC and TEFFSPECUNC.

There are seven methods used to estimate surface gravity by the SSPP. Application of the limits on $(g - r)_0$ and S/N eliminates a number of these estimates for any spectrum, and the biweight average of the log g estimates with indicator variables equal to 1 is taken for the final adopted surface gravity, named LOGGADOP. An estimate of the scatter around this value is also calculated, LOGGADOPUNC.

There are nine estimates of [Fe/H] in the SSPP. We adopt the validity ranges of S/N and $(g - r)_0$ in Table 3 to assign 1 or 0 as an indicator variable for each method and remove any estimate with indicator value 0 from further consideration. We then implement an additional outlier rejection procedure as follows. For each estimate, we generate a synthetic spectrum using the adopted $T_{\rm eff}$ and log g by interpolating within the grid of synthetic spectra used for the NGS1 estimate. We calculate a correlation coefficient (CC) and the mean of the absolute residuals (MAR) between the observed spectrum and synthetic spectrum in two different wavelength regions: 3850–4250 and 4500–5500 Å. These regions were selected to include the Ca II K and H lines and numerous metallic lines. We average the two metallicity estimates with the highest CCs and the two metallicity estimates with the lowest MARs, then from the remaining metallicity estimators we also select those within ± 0.5 dex of this average. In the next step, we compute an average $\mu_{\rm CC}$ ($\mu_{\rm MAR}$) and standard deviation $\sigma_{\rm CC}$ ($\sigma_{\rm MAR}$) of the CCs (MARs) for the surviving metallicity estimates from the previous step. As a final step to reject likely outliers, we select from the surviving metallicity estimates the ones with CC $> \mu_{\rm CC} - \sigma_{\rm CC}$ and MAR $< \mu_{\rm MAR} + \sigma_{\rm MAR}$. A biweight average is computed from the metallicity estimators that remain after this step and adopted as the final [Fe/H] named FEHADOP. Those metallicity estimators used in the final determination of the adopted [Fe/H] have their indicator variable set to 2. The MAR values have been added to the SSPP procedure since Lee et al. (2008a) in order to provide additional security that each method produces reasonable abundance estimates.

5.3. SSPP Flags

Because it is important that the SSPP identify situations where the quoted atmospheric parameters or the measured radial velocities may be in doubt, the SSPP raises a number of flags, which are listed in Table 2. These flags have been enhanced since SEGUE-1 (Yanny et al. 2009). FLAG is a five-letter code provided in a variable along with each set of parameter values for a spectrum that indicates possible issues with the determined stellar parameters and radial velocities.

The nominal condition for the five-letter flag combination is "nnnnn." This indicates that the SSPP is satisfied that a given stellar spectrum and its reported $g - r$ colors and S/N have passed all of the SSPP quality and consistency checks, and the stellar parameters should be considered well determined.

If Table 2 labels a flag value as "Critical," then if that flag is set, the SSPP either does not report atmospheric parameters for that star or, if the color flag is also raised, performs different steps from the normal processing. The color flag is defined as a "C" designation for the second letter. See Lee et al. (2008a) for

Table 4
Codes for INSPECT

Position	Flag[a]	Description
First	F	Fail: No parameters or radial velocity determined
Second	T	Temperature difference between TEFFADOP and IRFM $T_{\rm eff}$ is >500 K
Third	t	Temperature difference between TEFFADOP and spectroscopic-based $T_{\rm eff}$ > 500 K
Fourth	M	Adopted [Fe/H] and spectroscopic-based [Fe/H] is >+0.3
Fifth	m	Error in adopted [Fe/H] is >+0.3
Sixth	C	Low Confidence: correlation coefficient < 0.4

Note.
[a] The nominal code for all positions is "n."

details of the procedure for when the color flag is raised. Even when information is salvaged, the presence of a critical flag is a warning to the user to consider carefully possible effects and biases on the derived parameters.

On the other hand, the SSPP does report parameters for spectra with a "Cautionary" flag raised (see Table 2), because these flags indicate conditions that usually will not affect the determination of atmospheric parameters. There is a new flag "B" in the third position that is raised if the measured Hα strength is not within the expected range based on predictions from the Hδ line. However, Hδ cannot be measured reliably for stars cooler than about 5800 K because their Hδ lines are too weak. Therefore, the "B" flag should not be used to reject measurements for stars cooler than about 5800 K.

INSPECT is a six-letter code specified for each spectrum that alerts the user to possible issues that may be resolved by visual inspection including large discrepancies between the adopted value for a parameter and key contributors to that parameter, such as the IRFM temperature. The values for the INSPECT variable are given in Table 4. This variable is new for this version of the SSPP and its nominal value is "nnnnnn."

5.4. Data for SSPP Calibration and Evaluation

We "calibrate" the stellar parameters derived by the SSPP by comparing them to parameters for the same stars derived from independent observations or other external information. This comparison is used to remove any remaining systematic trends in the outputs of the SSPP that would otherwise lead to biased results that depend on the color, S/N, the metallicity, or other properties of the SEGUE stellar sample. The calibration set consists of SDSS/SEGUE stars reobserved at high resolution (Section 5.4.1), augmented with cluster stars with S/N > 50 (Section 5.4.2).

5.4.1. Higher-resolution Optical Sample

To establish parameters based on high-resolution spectra, a number of field stars observed with the SDSS spectrographs were reobserved at higher resolution. The derived parameters from the SSPP and high-resolution spectra for these stars, as well as their IDs in the SDSS database, are listed in Table 5. This field calibration sample consists of 128 stars observed with different spectrographs on several 8 m class telescopes. Spectra for 23 stars were collected with the High-Dispersion Spectrograph (HDS) (Noguchi et al. 2002) at the Subaru Telescope. These objects are primarily very-metal-poor

([Fe/H] $\leqslant -2.5$) stars near the main-sequence turnoff. The spectral coverage is from 4020 to 6732 Å, with $R \simeq 45{,}000$. Fourteen stars were observed with the Ultraviolet Visual Echelle Spectrograph (UVES; Dekker et al. 2000) at the VLT. The spectra cover (almost continuously) the range 3312–7908 Å and have $R \simeq 40{,}000$. Stars in the UVES sample are also typically rather warm, near the main-sequence turnoff. Keck Echellette Spectrograph and Imager (ESI; Sheinis et al. 2002) spectra were collected for 20 low-metallicity ([Fe/H] < -2) red-giant stars, with $R \simeq 6000$ and spectral coverage from 3900 to 10000 Å. The largest fraction of the field calibration sample, 57 stars covering a metallicity range from -2.7 to $+0.3$ and including both giants and dwarf stars, was observed with the High-Resolution Spectrograph (HRS; Tull 1998) at the Hobby–Eberly Telescope. The spectral coverage is from 4390 to 5910 Å, with $R \simeq 15{,}000$. Finally, Keck HIgh-Resolution Echelle Spectrometer (HIRES) data ($R \simeq 40{,}000$, wavelength range 3500–6400 Å) were collected for 14 stars. With the exception of two stars at [Fe/H] ~ -3.4, all of the stars in the HIRES sample have metallicities $-1 <$ [Fe/H] < 0. Previously, Allende-Prieto et al. (2008) analyzed the HRS data to assess the SEGUE-1 version of the SSPP, and an earlier analysis of some of this higher-resolution sample was used to evaluate the SEGUE-1 SSPP in Lee et al. (2008b). We present a reanalysis of the entire data set and a comparison with the SSPP parameters here.

For calibration of the DR9 SSPP values, all of the high-resolution spectra were reanalyzed homogeneously with MOOG (Sneden 1973; Sobeck et al. 2011) and Kurucz model atmospheres. Atmospheric parameters were determined by enforcing excitation and ionization balance: $T_{\rm eff}$ was adjusted to remove any slope of the Fe I abundance with excitation potential, and $\log g$ was altered to force agreement between Fe I and Fe II line abundances. When possible, Cr I/Cr II and Ti I/Ti II were used to confirm the $T_{\rm eff}$ and $\log g$ values found using iron lines. Microturbulent velocities were determined by forcing Fe abundances from strong and weak lines to agree; however, this method was not possible for the cool, metal-rich stars of our sample for which all lines were strong. As the majority of strong-lined stars were in the HRS subsample, we measured an empirical relation between $v_{\rm t}$ and $\log g$ for 33 stars in the (higher-resolution) Subaru and VLT subsamples. This relation, $v_{\rm t} = -0.345 \times \log g + 2.225$, was then used to fix the micro-turbulent velocities for the strong-lined stars in the HRS sample.

Uncertainties in the stellar parameters were determined in the following fashion: $T_{\rm eff}$, $\log g$, [Fe/H], and $v_{\rm t}$ were each altered by 250 K, 0.5 dex, 0.5 dex, and 0.5 km s^{-1}, respectively, while holding the other parameters fixed. The resulting differences in values were then added in quadrature to determine the parameter uncertainty. These errors are rather conservative. The results of this reanalysis are given in Table 5.

Note that the spectra in the HDS and UVES samples have a small number of lines because of their temperature and metallicity. The ESI sample has cooler stars in general but has fewer reliable lines because the spectra are much lower resolution. Therefore, the analysis of these stars is particularly challenging, and the derived errors are typically larger than those in different metallicity or temperature regimes.

5.4.2. Cluster Sample

Stars in globular and open clusters were observed with the SDSS spectrographs as part of the SEGUE-1 and SEGUE-2

Table 5
Comparison of Parameters from High-resolution and SSPP Analysis

Plate-MJD-Fiber	Spectrograph	High-resolution Analysis				DR9 Values[a]			$T_{\rm eff}$ IRFM[b]	S/N[b]
		$T_{\rm eff}$ (K)	log g (cgs)	[Fe/H]	$v_{\rm micro}$ (km s^{-1})	$T_{\rm eff}$ (K)	log g (cgs)	[Fe/H]	(K)	
0282-51658-530	VLT UVES	6200	3.55	−2.85	0.75	6196	3.497	−2.830	6243	27.3
0298-51955-485	SUBARU HDS	5350	3.65	−3.17	1.35	5690	3.544	−2.916	5582	54.3
0304-51609-528	SUBARU HDS	4990	3.25	−3.20	1.20	5315	2.679	−2.889	5217	25.9
0353-51703-605	HET HRS	5725	3.15	−0.66	1.40	6202	3.708	0.040	6208	62.3
0380-51792-236	HET HRS	6800	4.50	−0.24	0.70	6942	4.147	−0.285	6723	52.7
0390-51900-188	VLT UVES	6460	3.75	−3.05	1.25	6577	3.458	−3.132	6412	32.6
0396-51816-605	HET HRS	5325	4.00	−0.33	0.75	5401	4.461	−0.054	4690	51.6
0401-51788-407	HET HRS	4800	3.00	−0.55	1.55	4806	2.834	−0.321	4774	52.5
0401-51788-410	HET HRS	5500	4.25	−0.79	1.00	5751	4.039	−0.299	5845	51.8
0409-51871-449	HET HRS	5775	4.00	−0.10	1.00	5730	4.061	0.040	5809	59.0
0418-51884-574	VLT UVES	6375	3.60	−3.25	1.25	6677	3.619	−3.238	6480	61.5
0471-51924-613	VLT UVES	6375	3.40	−2.60	0.90	6207	3.384	−2.545	6208	48.3
0613-52345-280	HET HRS	5500	4.00	−1.13	0.85	5478	4.051	−0.698	5495	30.7
0681-52199-128	VLT UVES	6225	3.90	−2.85	0.75	6400	3.665	−2.896	6361	61.3
0711-52202-489	VLT UVES	5650	3.65	−3.27	1.00	5892	3.466	−3.248	5784	61.0
0726-52226-335	VLT UVES	6000	3.40	−2.52	0.90	6176	3.842	−2.666	6056	61.8
0732-52221-345	HET HRS	5100	3.60	−0.90	1.45	5184	3.317	−0.513	5150	52.7
0753-52233-013	VLT UVES	6075	3.95	−2.80	0.75	6287	3.550	−2.728	6220	60.0
0888-52339-599	HET HRS	6800	3.25	−0.60	1.00	7073	3.627	−0.356	7197	61.8
0889- 52663-204	HET HRS	6450	4.25	−0.65	0.80	6607	3.955	−0.375	6345	60.6
0913-52433-073	VLT UVES	6400	4.00	−2.70	1.10	6183	3.275	−3.045	6107	59.8
0952-52409-260	HET HRS	5325	4.00	−0.40	1.00	5765	4.256	−0.226	7245	59.9
0982-52466-480	SUBARU HDS	5610	3.05	−2.71	0.15	6323	3.476	−2.122	6215	61.9
1138-53228-626	HET HRS	5150	4.00	−2.74	1.00	5793	4.181	−2.393	5328	44.3
1185-52642-519	VLT UVES	6700	3.50	−2.83	0.60	6503	3.426	−3.330	6384	61.5
1323-52797-348	HET HRS	5800	3.90	−0.18	1.00	5821	3.697	−0.339	5824	90.5
1507-53763-303	KECK ESI	4850	1.85	−2.60	1.80	5091	2.061	−2.539	5090	21.6
1600-53090-378	VLT UVES	5900	4.10	−3.15	0.80	5963	3.131	−3.057	5959	36.0
1664-52973-216	KECK ESI	4900	1.90	−2.75	2.30	5062	2.248	−2.762	4976	36.4
1711-53535-285	VLT UVES	6050	4.50	−3.36	0.70	6511	3.869	−3.275	6330	70.2
1712-53531-636	VLT UVES	6300	4.60	−2.55	0.50	6384	3.396	−2.709	6265	52.8
1723-53905-430	VLT UVES	6000	4.00	−3.45	1.00	6314	3.733	−2.718	6200	52.2
1893-53239-104	KECK HIRES	6012	4.57	0.04	0.86	5947	3.990	−0.180	6006	48.7
1898-53260-369	KECK ESI	5050	1.80	−2.33	2.40	4956	1.261	−2.686	4985	76.7
1902-53271-029	KECK ESI	4450	0.50	−2.47	2.40	5091	1.855	−1.916	4787	35.1
1902-53271-605	KECK HIRES	4300	0.75	−3.46	1.71	4995	2.127	−2.556	4935	43.8
1905-53706-243	KECK HIRES	5825	4.02	−1.04	0.19	5915	4.320	−0.520	5816	63.1
1910-53321-398	KECK ESI	5150	2.25	−2.20	2.40	5267	1.607	−2.690	5267	57.0
1912-53293-352	SUBARU HDS	4320	4.80	−2.98	0.15	4733	3.867	−2.700	4655	111.8
1914-53729-357	SUBARU HDS	4740	0.85	−3.20	1.90	5244	2.159	−2.926	5148	101.7
1919-53240-173	KECK HIRES	6182	4.35	−0.04	1.21	6280	4.010	−0.060	6356	62.2
2041-53387-008	HET HRS	5425	3.50	−0.55	1.30	5509	3.401	−0.558	5405	31.5
2044-53327-122	HET HRS	5475	4.30	−0.90	1.00	5512	4.326	−0.705	5404	25.4
2044-53327-228	HET HRS	4600	1.50	−2.35	2.00	4846	1.478	−2.209	4849	48.9
2046-53327-061	SUBARU HDS	6275	3.90	−0.46	1.00	6524	4.033	−0.333	6484	49.5
2049-53350-020	HET HRS	5750	4.25	−0.21	0.75	5692	4.135	−0.541	5637	31.2
2049-53350-241	HET HRS	5600	3.70	−0.09	0.85	5559	3.707	−0.094	5646	55.1
2050-53401-288	KECK ESI	5275	2.00	−2.60	2.20	5231	2.139	−2.508	5313	36.8
2051-53738-595	KECK HIRES	5980	3.84	−0.58	1.00	6313	3.980	−0.400	6326	62.1
2052-53401-063	KECK HIRES	6230	3.99	−0.15	1.23	6342	3.820	−0.150	10981	62.1
2052-53401-533	HET HRS	6100	4.25	−0.50	0.80	6073	3.957	−0.157	6097	40.6
2052-53401-537	KECK HIRES	6002	3.86	−0.48	1.04	6399	4.000	−0.290	6623	62.8
2053-53446-023	HET HRS	6450	4.45	−0.10	0.50	6642	3.766	−0.357	6635	39.5
2053-53446-130	HET HRS	6000	4.00	−0.32	1.00	6254	3.996	−0.654	6267	33.9
2053-53446-171	HET HRS	6200	3.75	−0.87	1.00	6350	3.635	−0.750	6470	52.3
2053-53446-226	HET HRS	6600	3.85	−0.54	0.70	6786	3.905	−0.465	6756	93.2
2053-53446-346	HET HRS	6400	4.00	−0.68	1.00	6783	3.893	−0.373	6859	49.0
2053-53446-505	HET HRS	6800	4.70	−0.20	0.50	6711	4.035	−0.288	6653	65.1
2054-53431-033	SUBARU HDS	4640	0.70	−3.17	2.05	5162	2.384	−2.845	5107	84.1
2054-53431-056	HET HRS	6800	4.00	−0.50	0.75	6872	3.829	−0.217	6834	27.8
2054-53431-070	KECK HIRES	4675	1.55	−3.32	1.27	5279	2.242	−2.601	5296	62.7
2054-53431-259	HET HRS	6600	3.65	−0.65	0.85	6784	3.606	−0.298	6833	56.6

Table 5
(Continued)

Plate-MJD-Fiber	Spectrograph	High-resolution Analysis				DR9 Values[a]			$T_{\rm eff}$ IRFM[b]	S/N[b]
		$T_{\rm eff}$ (K)	$\log g$ (cgs)	[Fe/H]	$v_{\rm micro}$ (km s^{-1})	$T_{\rm eff}$ (K)	$\log g$ (cgs)	[Fe/H]	(K)	
2054-53431-280	HET HRS	6000	3.55	−0.57	1.00	6394	3.812	−2.118	6379	58.2
2054-53431-552	HET HRS	6200	3.70	−0.72	1.00	6393	3.721	−0.785	6183	51.3
2056-53463-362	KECK ESI	5125	2.50	−3.00	1.80	5166	2.899	−3.259	4993	31.8
2056-53463-541	HET HRS	6000	4.10	−0.09	1.00	6904	3.931	−0.141	6946	61.1
2068-53386-085	HET HRS	6250	4.65	−1.06	1.00	6070	3.934	−0.076	6032	52.4
2068-53386-151	KECK HIRES	5518	3.82	−0.58	0.53	5837	4.000	−0.520	5918	61.8
2070-53729-084	KECK HIRES	6000	4.50	0.09	1.07	6151	4.050	0.030	6050	53.1
2078-53378-003	HET HRS	5170	1.50	−2.02	2.00	5492	2.072	−1.902	5694	56.0
2078-53378-014	HET HRS	5620	4.10	−0.54	1.00	5752	3.585	−0.609	5549	56.5
2078-53378-038	HET HRS	6500	4.30	−0.92	1.00	6778	3.942	−0.092	6770	56.3
2078-53378-040	HET HRS	6350	3.90	0.03	1.00	6659	3.743	−0.208	6688	70.4
2078-53378-044	HET HRS	6150	4.25	−0.57	1.00	6606	3.711	−0.143	6557	59.7
2078-53378-049	HET HRS	6250	3.90	−0.46	1.00	6445	3.784	−0.506	6467	40.2
2078-53378-136	HET HRS	5820	2.60	−0.82	1.50	6330	3.675	−0.799	6184	55.7
2078-53378-289	HET HRS	6400	3.50	−0.49	0.80	6835	3.892	−0.300	6798	25.6
2078-53378-598	HET HRS	5960	3.45	−0.54	1.00	6404	3.869	−0.672	6438	40.9
2079-53379-040	HET HRS	6400	3.65	0.31	1.00	6659	3.662	−0.198	6689	49.1
2176-54243-614	SUBARU HDS	5550	4.45	−2.50	1.70	5451	2.695	−2.853	5455	61.3
2178-54629-546	SUBARU HDS	5290	3.00	−2.81	1.50	5416	2.591	−2.821	5523	65.7
2181-53524-218	HET HRS	5280	4.15	−0.12	1.00	5532	4.192	−0.087	5600	48.4
2181-53524-358	HET HRS	5200	3.55	−0.40	1.00	5351	3.396	−0.862	5337	32.9
2182-53905-329	KECK ESI	5200	2.50	−2.00	2.20	5150	2.369	−2.309	5156	45.8
2182-53905-577	KECK ESI	5150	2.50	−2.20	2.25	5183	1.636	−2.386	5346	55.4
2183-53536-131	HET HRS	5600	3.80	0.27	1.00	5544	3.787	0.144	5641	58.6
2183-53536-175	SUBARU HDS	5480	3.05	−2.66	1.55	5370	2.665	−2.671	5315	64.4
2183-53536-197	HET HRS	6000	3.90	−0.60	1.00	6039	3.561	−0.703	5990	52.3
2184-53534-058	SUBARU HDS	6050	4.70	−2.67	1.00	6219	4.124	−2.469	6489	32.7
2184-53534-083	HET HRS	5940	3.80	0.06	1.00	6053	3.829	−0.168	6115	40.7
2184-53534-107	HET HRS	5100	2.90	−1.05	1.00	5128	2.455	−1.423	5113	56.8
2184-53534-120	SUBARU HDS	4800	1.65	−2.57	1.60	4970	1.614	−2.636	5055	67.2
2184-53534-136	SUBARU HDS	5780	4.00	−0.85	0.40	5968	3.836	−0.895	6136	54.4
2184-53534-413	HET HRS	5020	3.35	0.01	1.10	5449	4.353	−0.009	5595	47.7
2184-53534-429	HET HRS	5900	3.85	−1.83	2.00	6274	4.180	−1.454	6273	51.0
2184-53534-451	HET HRS	5640	3.75	−0.45	1.00	6266	3.962	−0.387	6346	31.1
2248-53558-060	HET HRS	5700	4.00	−0.28	1.00	5799	3.995	−0.324	5745	51.8
2248-53558-221	HET HRS	5700	3.50	−1.06	1.00	6105	3.971	−1.103	6251	27.1
2248-53558-247	HET HRS	6050	3.30	−0.22	1.50	6459	3.710	−0.229	6566	46.0
2248-53558-345	HET HRS	5120	3.65	0.07	1.00	5509	4.452	−0.148	5814	74.2
2251-53557-279	SUBARU HDS	6290	4.05	−2.15	1.05	6498	3.455	−2.100	6433	66.6
2251-53557-305	HET HRS	5200	3.60	−0.92	1.20	5307	3.572	−0.850	5286	43.7
2303-54629-154	KECK ESI	4900	1.90	−2.01	1.80	4841	1.884	−2.294	4858	53.9
2303-54629-174	KECK ESI	4900	2.40	−2.58	2.20	5241	2.847	−2.648	5225	63.4
2307-53710-074	KECK HIRES	5800	4.16	−0.29	0.65	5971	4.080	−0.370	6048	54.5
2307-53710-386	KECK HIRES	5985	3.87	−0.80	1.57	6277	4.240	−0.530	6328	23.9
2309-54441-277	KECK ESI	4750	1.35	−2.32	1.85	5126	2.051	−2.232	5026	61.5
2309-54441-564	SUBARU HDS	4550	0.90	−3.21	2.30	5060	1.985	−2.900	4936	64.0
2311-54331-231	KECK ESI	5100	1.85	−2.61	1.70	5174	2.056	−2.687	5224	61.6
2313-53726-207	KECK ESI	4550	0.60	−2.27	2.35	4633	1.362	−2.535	4660	60.7
2313-53726-624	KECK ESI	4900	1.45	−2.65	1.75	5021	1.397	−3.037	5001	60.5
2314-53713-090	SUBARU HDS	6860	4.90	−2.78	0.90	6799	3.883	−2.860	6644	26.3
2328-53728-059	KECK HIRES	5995	4.19	−0.09	1.00	6097	3.970	−0.050	6101	53.6
2335-53730-542	KECK HIRES	5982	3.95	−0.79	1.08	6390	3.920	−0.520	6368	49.1
2336-53712-052	HET HRS	4620	1.90	−0.48	1.50	4859	2.412	−0.534	4796	43.8
2452-54178-219	KECK ESI	5300	2.25	−1.90	2.00	5366	2.427	−2.098	5317	50.0
2476-53826-575	SUBARU HDS	4430	0.65	−2.62	1.80	5036	1.668	−2.219	7294	68.5
2622-54095-483	SUBARU HDS	4380	0.45	−3.73	2.35	4769	1.645	−3.405	4680	65.7
2677-54180-345	KECK ESI	4875	1.70	−2.70	2.00	5227	2.342	−2.615	5198	53.0
2689-54149-292	SUBARU HDS	4890	2.20	−2.71	1.50	5159	2.573	−2.745	5075	67.8
2689-54149-526	KECK ESI	4700	1.30	−2.51	2.50	4855	1.517	−2.553	4895	53.9
2797-54616-273	KECK ESI	5200	2.25	−2.50	2.00	5237	1.795	−2.374	5336	56.3
2799-54368-138	SUBARU HDS	5540	2.80	−2.05	0.05	5325	1.800	−3.381	5271	83.2
2799-54368-502	SUBARU HDS	4720	1.95	−3.69	1.70	5296	2.734	−3.069	5205	51.7

Table 5
(Continued)

Plate-MJD-Fiber	Spectrograph	High-resolution Analysis				DR9 Values[a]			$T_{\rm eff}$ IRFM[b]	S/N[b]
		$T_{\rm eff}$ (K)	$\log g$ (cgs)	[Fe/H]	$v_{\rm micro}$ (km s^{-1})	$T_{\rm eff}$ (K)	$\log g$ (cgs)	[Fe/H]	(K)	
2799-54368-560	SUBARU HDS	5100	2.65	−3.00	1.05	5461	2.968	−2.870	5376	43.6
2815-54414-323	KECK ESI	4500	1.65	−2.85	1.80	4756	1.422	−2.175	4807	61.9
2848-54453-059	SUBARU HDS	4710	1.55	−3.01	1.70	5074	1.815	−2.961	5077	53.1
2897-54585-210	SUBARU HDS	4850	1.75	−3.04	1.80	5178	2.408	−2.898	5204	52.2

Notes.
[a] Adopted SSPP parameters FEHADOP, LOGGADOP, and TEFFADOP, from the Catalog Archive Server sppParams table.
[b] Measured using the high-resolution spectrum.

(This table is available in machine-readable form.)

surveys. These clusters span the metallicity range $-2.5 \leqslant$ [Fe/H] $\leqslant +0.3$. The cluster members used for further analysis are listed in Table 6 and were selected with a CMD-mask algorithm using the SDSS photometry and cuts in RV, proper motion, and metallicity. The detailed procedures to identify the member stars in each cluster field are described in Lee et al. (2008b) and Smolinski et al. (2011), and we refer the interested reader to those papers. Note that the cluster membership criteria used by Smolinski et al. (2011) and Morrison et al. (2016) differ slightly: Morrison et al. (2016), whose major interest was the giant stars in each cluster, used proper-motion criteria for membership but did not use the SSPP [Fe/H] values. While most of the GCs in the sample are known to display variations in the CN band strength down to the main sequence (see, e.g., Cohen et al. 2005; Smith & Briley 2006), the effects on the derived $T_{\rm eff}$, $\log g$, [Fe/H], and $v_{\rm rad}$ are negligible. This is because the SSPP uses features that, at the typical C and N content found in GC stars, are not affected by CN, CH, and NH lines. The effects of dispersion in other light elements (like Na, Mg, and Al; see e.g., Kraft 1994) are even smaller.

Stars with S/N > 50 in Table 6 were used to calibrate SSPP metallicities (see Section 5.5). Because the members observed in low-metallicity globular clusters were usually giants, while those in solar-metallicity clusters were dwarfs, cluster stars were not used for the $\log g$ calibration. They were also not used for the $T_{\rm eff}$ calibration because their SDSS photometry was often saturated, unlike that for the fainter field stars.

5.5. Calibration of SSPP Values

The parameters derived for the calibration sample of 128 stars with high-resolution spectra were used for final calibration of the SSPPs estimates of effective temperature, surface gravity, and metallicity. For the metallicity calibration, the high-resolution sample is augmented by cluster members. Here, the final calibration of each method in the SSPP is briefly described.

For each of the nine temperature estimates, we compute the difference between the estimates of each method and the IRFM temperature estimates from the SDSS/SEGUE high-resolution sample. We then fit a quadratic function to the offset as a function of $T_{\rm eff}$ and use this relation to apply a correction to all the $T_{\rm eff}$ estimates reported by the SSPP. Only 107 stars were available for the temperature comparison, as only those 107 stars have J-, H-, and K-band photometry available.

There are seven estimators of $\log g$ considered when computing the final adopted $\log g$. For each of the seven methods, we fit a linear relation to the offset between the SSPP

estimate and the value of $\log g$ determined from the high-resolution spectra. This relation is used to correct the $\log g$ estimates reported by the SSPP.

There are nine metallicity estimators used to compute the final adopted metallicity, as indicated in Table 3. Because the high-resolution sample does not include stars with [Fe/H] ~ -1.5 and [Fe/H] > 0.0, we added cluster members to the calibration sample. These are stars in clusters with known metallicity and that have SDSS/SEGUE spectra with S/N > 50. We note that these cluster stars are all red giants at [Fe/H] ~ -1.5 and dwarfs at [Fe/H] > 0, and the APOGEE-SEGUE overlap sample gives us an additional source of external validation of the SSPP parameters for stars in these parameter ranges (Section 6.3.2). For each SSPP metallicity estimator, we fit a quadratic relation to the difference between the SSPP value and the metallicity determined from the high-resolution spectrum or, for cluster stars, the known literature value as tabulated in Smolinski et al. (2011). We use this quadratic relation to correct the SSPP metallicity estimates.

As examples of the results of this procedure, Figure 8 shows the correction functions for two selected methods: NGS1 (left) and ANNRR (right). The red curve and line indicate the correction functions, which are derived from a quadratic fit for the temperature and metallicity, and a linear fit for the gravity.

Figure 9 displays the difference between the adopted [Fe/H] measured for the SDSS/SEGUE spectra using the SSPP, after this final calibration step, and the same parameters measured with the high-resolution observations of the same stars. Complete information for all the parameters is in Table 5. From the analysis of the $\log g$ residuals in Table 5, the SSPP estimates of $\log g$ are useful for separating giants from dwarfs but are not as accurate as the $\log g$ estimated from the high-resolution spectra; we reach the same conclusion when comparing with APOGEE (see Section 6.3.2). Looking at Figure 9, there are no significant systematic trends in the SSPP metallicities with $T_{\rm eff}$ or $\log g$. At the extremes of the metallicity distribution, a regime where low-resolution spectroscopy typically performs poorly, there is a small systematic underestimate of [Fe/H] for high-gravity stars with [Fe/H] $\gtrsim 0$. We find a similar trend for dwarf stars with [Fe/H] $\gtrsim 0$ when we compare with APOGEE (Section 6.3.2).

6. SSPP Parameter Validation and Error Estimation

6.1. Parameter Errors

We determine the precision and accuracy of the SSPP parameters using internal and external comparison data. We

Table 6
List of Cluster Members (Abridged)

| Cluster	Plate	MJD	Fiber	T_{eff} (K)	log g (cgs)	[Fe/H] (dex)	$g - r$	S/N	R.A. (deg)	Decl. (deg)
M92	2247	54,169	362	5491	2.54	−2.185	0.450	25.0	259.04869	43.060083
M92	2247	54,169	364	5405	3.23	−2.404	0.492	37.5	259.08213	43.240253
M92	2247	54,169	367	5404	2.85	−2.168	0.486	36.8	259.10185	43.195661
M92	2247	54,169	379	6428	3.55	−2.393	0.250	19.1	259.22175	42.998355
M92	2247	54,169	380	5299	2.64	−2.322	0.496	38.8	259.12453	43.100900
M92	2247	54,169	404	5353	2.27	−2.397	0.496	38.5	259.14868	43.202531
M92	2247	54,169	408	5210	1.67	−2.408	0.496	49.8	259.1516	43.115600
M92	2247	54,169	418	5234	2.31	−2.249	0.497	49.1	259.19255	43.082900
M92	2247	54,169	444	5347	2.50	−2.356	0.495	45.2	259.17824	43.246500
M92	2247	54,169	449	5232	1.82	−2.283	0.496	48.3	259.20122	43.171300
M92	2247	54,169	451	5374	2.79	−2.224	0.498	42.4	259.26814	43.069600
M92	2247	54,169	452	5330	2.24	−2.336	0.536	44.3	259.18977	43.229588
M92	2247	54,169	458	5704	2.87	−2.305	0.411	19.9	259.20611	43.215067
M92	2247	54,169	484	5076	2.16	−2.455	0.619	51.4	259.14905	42.944266
M92	2247	54,169	504	5205	1.99	−2.315	0.499	50.6	259.34715	42.948800
M92	2247	54,169	514	5545	1.79	−2.329	0.427	23.1	259.29469	42.900647
M92	2247	54,169	516	5694	2.42	−2.502	0.433	19.9	259.32981	42.963441
M92	2247	54,169	519	5727	3.81	−2.225	0.451	18.6	259.29888	42.918094
M92	2247	54,169	529	5472	3.27	−2.352	0.494	28.6	259.24274	43.260229
M92	2247	54,169	531	5350	2.76	−2.244	0.528	38.4	259.31297	43.264529
M92	2247	54,169	538	5903	2.61	−2.122	0.385	16.4	259.34134	43.258036
M92	2247	54,169	541	5623	3.03	−1.969	0.413	21.5	259.43884	43.035659
M92	2247	54,169	546	5430	2.03	−2.525	0.475	28.7	259.35424	43.022882
M92	2247	54,169	561	5415	2.95	−2.473	0.499	37.7	259.34981	43.120200
M92	2247	54,169	563	5283	2.35	−2.214	0.500	48.6	259.32958	43.215200
M92	2247	54,169	573	5416	2.83	−2.317	0.498	43.7	259.32140	43.074200
M92	2247	54,169	575	5712	3.78	−2.258	0.443	15.3	259.38118	43.246889
M92	2247	54,169	581	5358	1.99	−2.257	0.499	37.5	259.39378	43.071100
M92	2247	54,169	582	7429	3.48	−2.098	0.025	50.2	259.43614	43.099738
M92	2247	54,169	584	5568	2.27	−2.478	0.444	18.9	259.48440	43.059528
M92	2247	54,169	589	5354	2.29	−2.351	0.487	30.0	259.43215	43.063400
M92	2247	54,169	608	5163	2.34	−2.407	0.609	48.2	259.45984	43.229468
M92	2247	54,169	610	5106	2.08	−2.365	0.637	50.8	259.51967	43.171192
M92	2247	54,169	616	5714	3.09	−2.245	0.459	19.9	259.39054	43.189591
M92	2247	54,169	620	5471	2.25	−2.334	0.486	23.3	259.43737	43.135584
M92	2256	53,859	513	5590	2.56	−2.319	0.427	25.4	259.29469	42.900647
M92	2256	53,859	522	6078	3.45	−2.571	0.327	18.0	259.21141	43.231249
M92	2256	53,859	530	6489	3.98	−2.017	0.276	13.4	259.36776	43.250743
M92	2256	53,859	535	6350	3.80	−2.385	0.310	16.6	259.31357	43.280811
M92	2256	53,859	536	6295	3.63	−2.209	0.287	18.9	259.28945	43.280228
M92	2256	53,859	538	5560	3.50	−2.533	0.480	24.7	259.38004	43.210475
M15	1960	53,289	401	5244	2.53	−2.33	0.528	55.9	322.45217	12.338844
M15	1960	53,289	402	5101	2.09	−2.391	0.590	62.2	322.46795	12.327691
M15	1960	53,289	406	5130	1.75	−2.426	0.581	65.1	322.41683	12.266688
M15	1960	53,289	411	5385	2.78	−2.577	0.474	48.8	322.40463	12.227963
M15	1960	53,289	413	5241	1.97	−2.451	0.542	57.6	322.41431	12.305799
M15	1960	53,289	419	5119	2.28	−2.472	0.578	65.1	322.45799	12.303373
M15	1960	53,289	420	6068	3.48	−2.007	0.305	15.0	322.65913	12.145007
M15	1960	53,289	441	5563	2.57	−2.273	0.439	23.7	322.59754	12.257596
M15	1960	53,289	442	5286	2.27	−2.328	0.516	46.8	322.50280	12.375646
M15	1960	53,289	457	5552	2.10	−2.264	0.403	20.3	322.53153	12.31268
M15	1960	53,289	459	5319	1.94	−2.314	0.495	68.2	322.70535	12.125361
M15	1960	53,289	460	5421	2.80	−2.366	0.452	47.8	322.72679	12.119604
M15	1960	53,289	500	5525	2.81	−2.253	0.433	35.4	322.42966	12.004886
M15	1960	53,289	501	5839	2.80	−2.115	0.384	16.5	322.56493	11.992488

(This table is available in its entirety in machine-readable form.)

first assess the internal consistency and repeatability of the SSPP values across the range of stellar parameters and S/N in the SDSS/SEGUE data. We do this using SSPP measurements for repeat SDSS/SEGUE observations of the same stars. To evaluate the absolute accuracy of the SSPP metallicity estimates, we use the complete list of cluster stars listed in Table 6. The cluster sample spans a range of [Fe/H] from −2.35 to +0.30 and is described in Section 5.4.2. As an additional external evaluation, we compare the SSPP values to those measured by the APOGEE survey (Majewski et al. 2017)
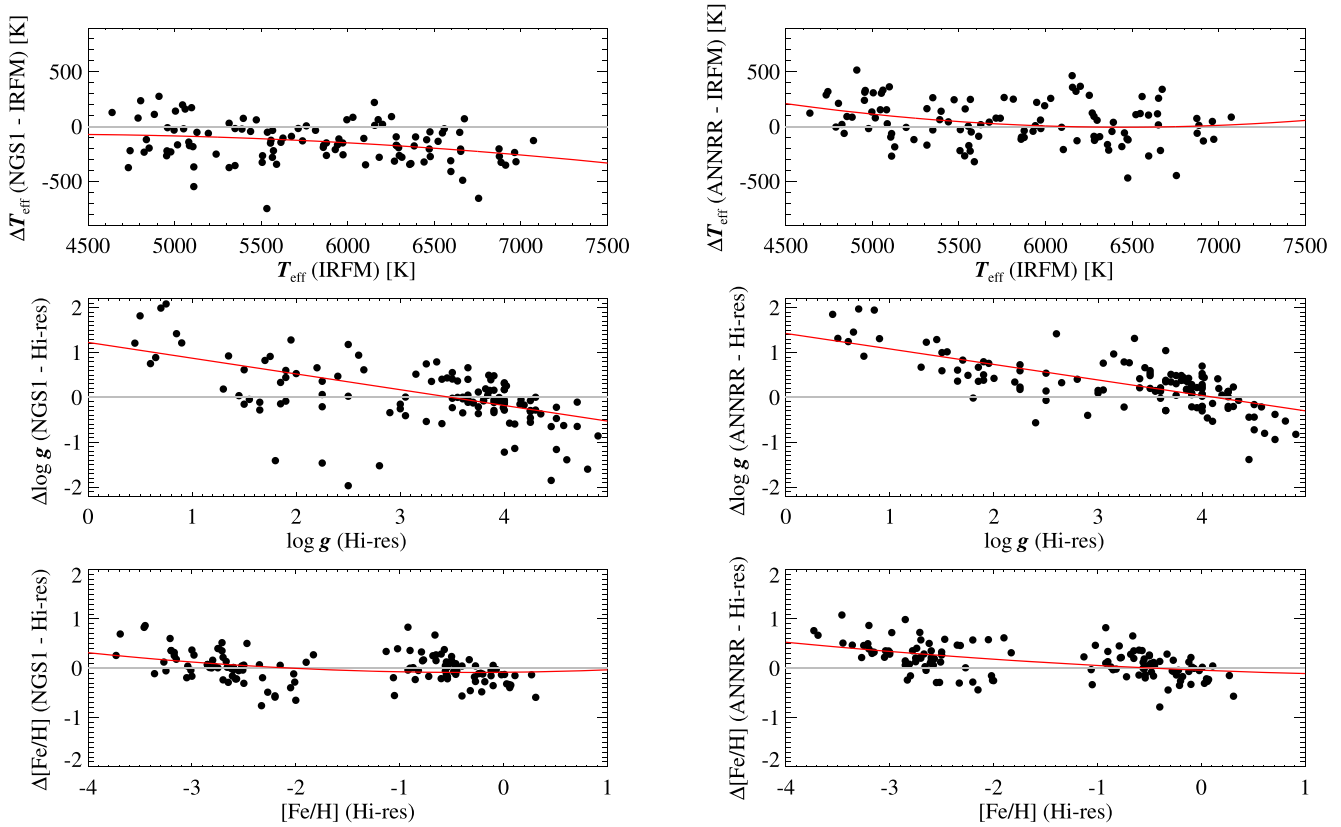
Figure 8. Two examples of correction functions (red curves and lines) from NGS1 (left panels) and ANNRR (right panels). The correction function for the temperature and metallicity is derived from a quadratic fit, whereas a linear fit is used for gravity.
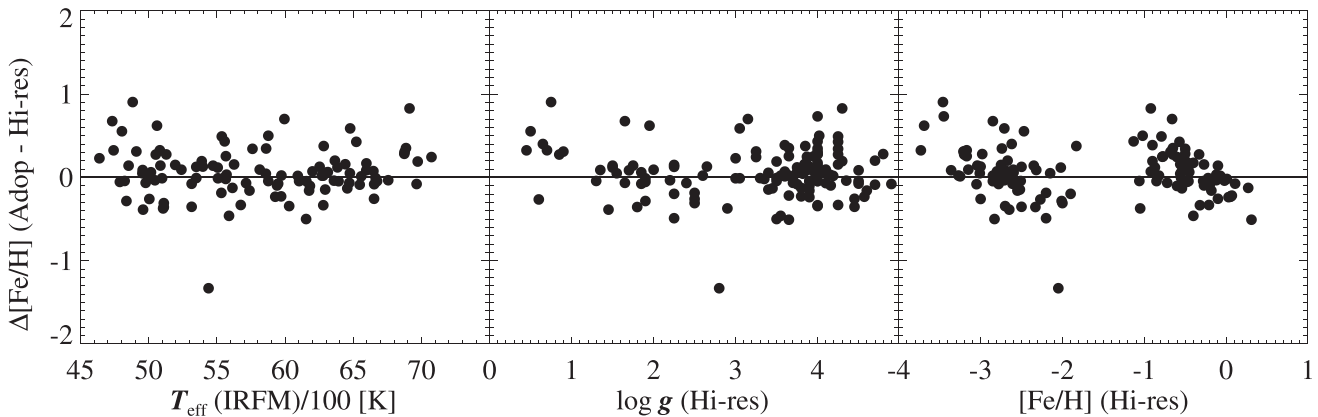

Figure 9. Comparisons of adopted SSPP measurement of [Fe/H] with values from the high-resolution analysis, as a function of each parameter.

using the subset of SDSS/SEGUE stars observed by both surveys as of Data Release 14 (Abolfathi et al. 2018, DR14).

The results of the internal comparison are shown in Figure 10 and summarized in Table 7. The comparison with APOGEE is summarized in Table 8. The mean (note, not the mean offset) and standard deviation values for the comparison with the cluster stars are given in the right panels of Figure 11. Figure 12 summarizes the comparison of the measured mean [Fe/H] in the right panels of Figure 11 with the literature values of [Fe/H] in the left panels.

We summarize the results of this section here and give more details below. For [Fe/H], comparison with the cluster stars and APOGEE are consistent with a scatter of 0.10–0.15 dex for most stars (Tables 7, 8, Figure 11). The scatter in the SSPP [Fe/H] comparisons depends on both [Fe/H] and $T_{\rm eff}$ and is largest for the bluest, most metal-poor stars (Table 7). The [Fe/H] parameter determinations are accurate over the full range of the cluster sample, $-2.35 <$ [Fe/H] < 0.3 (Figure 12). The SSPP [Fe/H] values for dwarf stars near solar metallicity, [Fe/H] > -0.2, have a mean offset relative to estimates from the SEGUE high-resolution spectra and APOGEE of about -0.15 dex (Figure 14). Internal repeatability estimates of SSPP $T_{\rm eff}$ give an rms scatter of 33–76 K, depending on the temperature and metallicity of the stars (Table 7). The SSPP
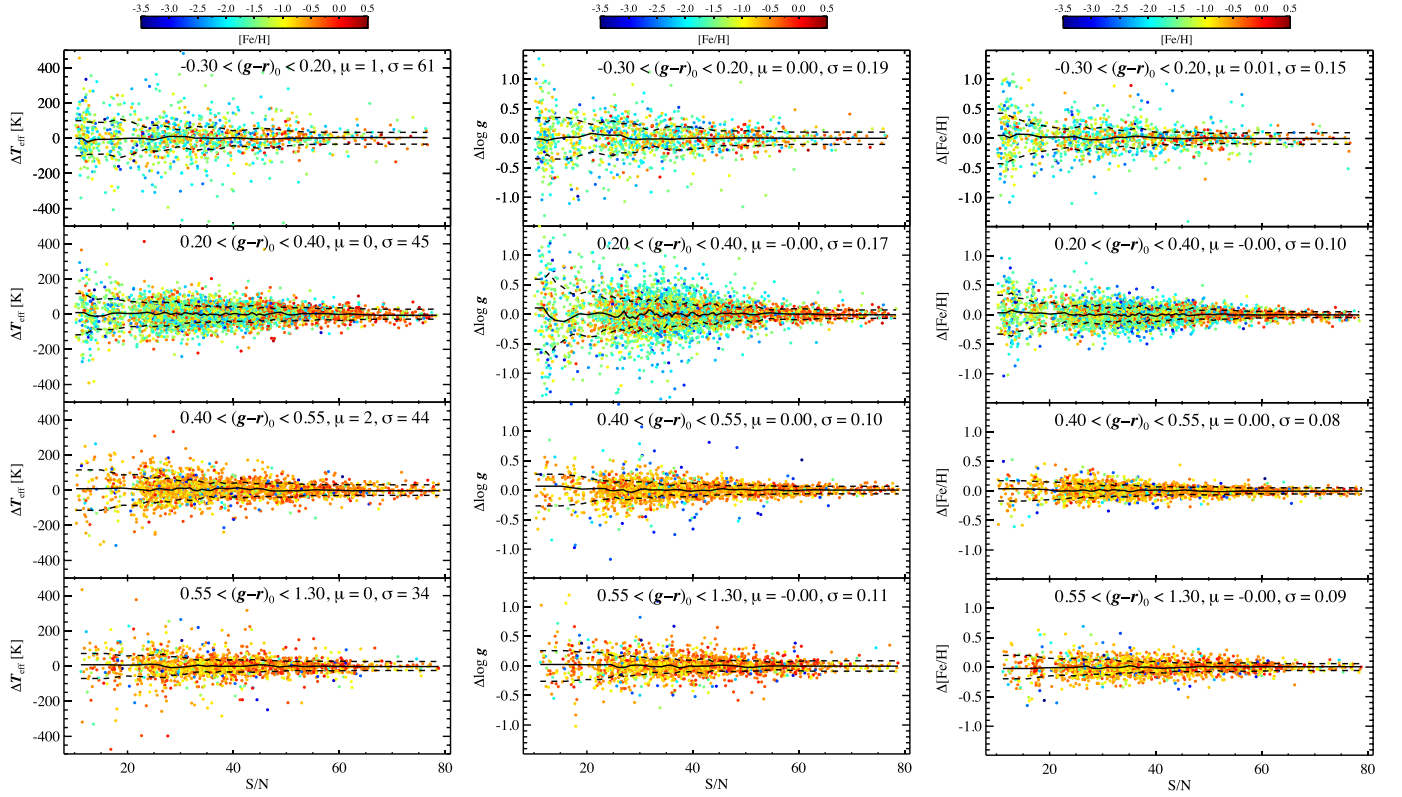
Figure 10. Residual distribution of T_{eff}, $\log g$, and [Fe/H] for repeat observations as a function of S/N. The sample of repeat observations is split into four different regions of $(g - r)_0$. The $(g - r)_0$ color range in the panels runs from blue at the top to red at the bottom. The dashed line denotes one Gaussian sigma as computed for bins of 200 stars ordered by S/N. See also Table 7.

Table 7
rms Values for Internal Comparisons

$(g - r)_0$	[Fe/H]	$\sigma(T_{eff})$ (K)	$\sigma(\log g)$ (dex)	$\sigma([Fe/H])$ (dex)
$-0.30 < (g - r)_0 < 0.20$	$-4.0 <$ [Fe/H] < -1.5	76	0.23	0.22
$-0.30 < (g - r)_0 < 0.20$	$-1.5 <$ [Fe/H] $< +0.5$	53	0.19	0.14
$0.20 < (g - r)_0 < 0.40$	$-4.0 <$ [Fe/H] < -1.5	48	0.26	0.15
$0.20 < (g - r)_0 < 0.40$	$-1.5 <$ [Fe/H] $< +0.5$	43	0.15	0.11
$0.40 < (g - r)_0 < 0.55$	$-4.0 <$ [Fe/H] < -1.5	60	0.35	0.15
$0.40 < (g - r)_0 < 0.55$	$-1.5 <$ [Fe/H] $< +0.5$	43	0.12	0.10
$0.55 < (g - r)_0 < 1.30$	$-4.0 <$ [Fe/H] < -1.5	60	0.26	0.18
$0.55 < (g - r)_0 < 1.30$	$-1.5 <$ [Fe/H] $< +0.5$	33	0.12	0.11

Table 8
Comparison with APOGEE Parameters

Parameter	Offset[a]	rms	No. of Stars
$\log g$	0.08 dex	0.25 dex	330
[Fe/H]	-0.06 dex	0.15 dex	568
Radial velocity	3.65 km s^{-1}	3.75 km s^{-1}	546

Note.
[a] Offset is computed as the mean of the SEGUE-2 parameter values minus the mean of the APOGEE parameter values.

$\log g$ estimates are useful for separating dwarfs from giants but are not as accurate as the $\log g$ estimates from high-resolution data like APOGEE (Table 9, Figure 13). We give more details on these comparisons below.

6.2. Internal Uncertainties Based on Repeat Observations

We estimate the internal uncertainty and repeatability of the SSPP parameters using stars that have more than one spectroscopic observation over the entire SDSS, SEGUE-1, and SEGUE-2 surveys. We require that both observations have S/N per ~ 1 Å pixel of $\geqslant 10$ in order to have reliable SSPP parameter estimates for each spectrum. We also require the difference in the S/N for the two spectra in each pair be closer than ± 10, the SSPP flag for each spectrum to be "nnnnn," the correlation coefficient between the best-fit synthetic spectrum and the observed spectrum be larger than zero, no bad pixels (inverse variance $= 0$) in the spectra, and the availability of valid stellar parameters for both spectra in each pair of repeat observations. There are ~ 9000 stars with repeat observations that pass these criteria.
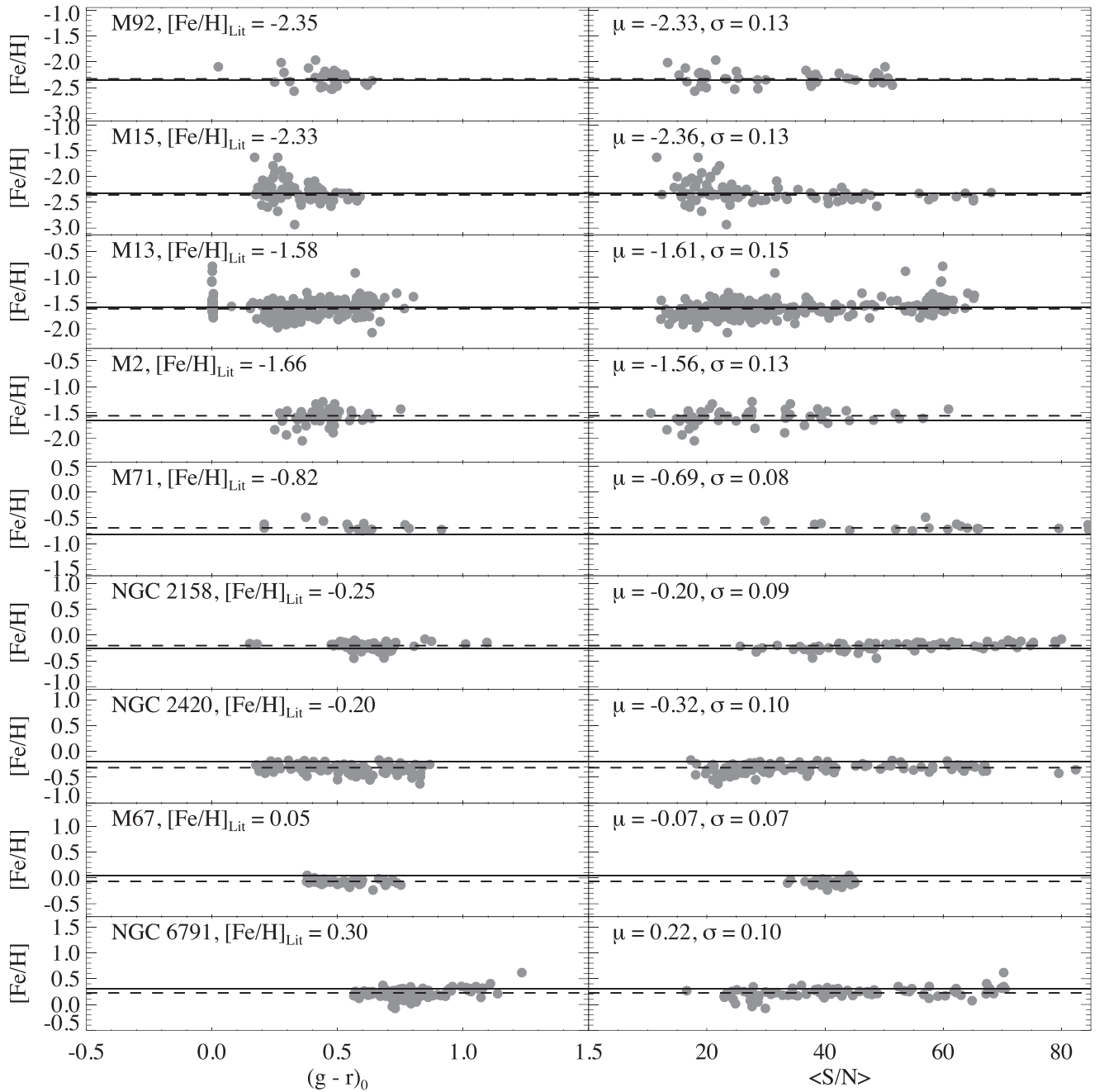
Figure 11. Run of [Fe/H] as a function of $(g − r)_0$ (left panels) and average signal-to-noise ratio $\langle S/N \rangle$ per angstrom (right panels) for member stars of open and global clusters. The Gaussian mean (μ) and standard deviation (σ) of the SEGUE SSPP parameter values are listed in the right panels. [Fe/H]$_{Lit}$ indicates the literature value used for our comparison and plotted as a solid line, while our derived value is the dashed line.

We use the parameter estimates for these duplicate observations to update the internal uncertainties of the SSPP quoted for earlier versions of the SSPP in Lee et al. (2008a) and Yanny et al. (2009). The distribution of the differences for the parameters is shown in Figure 10. The repeatability of the measurements depends on the number and strength of the spectral lines, as well as on the S/N, and at fixed S/N is a strong function of stellar temperature and metallicity. In Table 7 we report the standard deviation of the differences between the two measurements of each parameter for the same object. To account for the dependence on stellar properties, we report the standard deviation of the differences in each of four different bins of $(g − r)_0$ and two metallicity ranges ([Fe/H]

$< −1.5$ and [Fe/H] $> −1.5$). These empirical measurements of the rms scatter of repeat observations are most representative of the true internal uncertainty in the SSPP parameter estimates. In contrast, the formal errors reported by the SSPP[30] are nearly always smaller than the more realistic uncertainties computed here based on the repeat observations. The estimates of the internal parameter uncertainties in Table 7 and Figure 10 should be used in preference over the formal values computed by the SSPP.

---

[30] And given in the SDSS database as the UNC values for each SSPP parameter estimator in the sppParams table, e.g., FEHANNSRUNC.
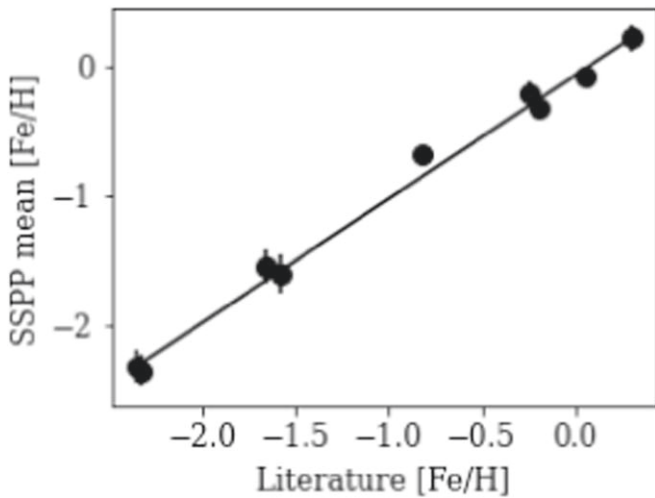
Figure 12. Summary of SEGUE SSPP cluster sample [Fe/H] measurements compared with literature values. The literature values are as given in the left panels of Figure 11. The SSPP-measured mean [Fe/H] values for the SEGUE cluster sample are given in the right panels of Figure 11. The vertical error bars are the size of the standard deviation of the [Fe/H] measurements for the SEGUE sample, also shown in the right panels. There is no systematic trend in the comparison over the entire metallicity range of the cluster sample.

6.3. Uncertainties from Comparisons with Cluster and APOGEE Data

For external validation of the SSPP parameters, we used the metallicities determined for individual cluster members observed with SEGUE, as well as parameters derived for the stars observed in both the SEGUE survey and the APOGEE survey. These external comparisons allow us to estimate the systematic uncertainties in the SSPP values.

6.3.1. Metallicities of Cluster Stars

The globular and open cluster data (see Section 5.4.2) span a broad range in [Fe/H] and $T_{\rm eff}$ over which we can evaluate the accuracy of the SSPP. However, the cluster data also span a range in S/N because the multiplex SDSS/SEGUE observations of the cluster stars had fixed exposure times for the wide range in apparent magnitude spanned by the cluster targets.

Figure 11 shows DR9 SSPP metallicity determinations for cluster stars as a function of color and S/N. The mean and standard deviation of the SSPP metallicities for each cluster are given in the right panels. The solid line indicates the literature value for each cluster listed in the left panels, and the dashed line denotes the mean value of the relevant parameter for each cluster as measured by the SSPP. The metallicity estimates are accurate for stars in clusters from metal poor to super metal rich with small scatter. The rms scatter is about 0.10 dex for [Fe/H] > −1, increasing to 0.13 dex for the metal-poor clusters M2, M13, and M92. Moreover, there are no discernible trends with either S/N or $(g - r)_0$ despite the range of log g and $T_{\rm eff}$ spanned by many of the cluster samples. We note that the larger scatter for the extreme BHB stars in M13 is because the SDSS photometric pipeline did not provide *ugriz* photometry for these stars in the crowded cluster field (An et al. 2008). Some SSPP methods of parameter determination, particularly for hot stars, require accurate photometry, degrading the accuracy of the BHB estimates in this case. The comparison of the SSPP [Fe/H] measurements

for the cluster sample with literature values is summarized in Figure 12. There is no significant systematic trend in the SSPP mean [Fe/H] measured for each cluster over the entire range of metallicity from the old, metal-poor globular cluster M92 at [Fe/H] = −2.35 to the open cluster NGC 6791 at [Fe/H] = +0.3.

6.3.2. Higher-resolution NIR Spectra from the APOGEE Survey

The APOGEE survey (see Section 2.2) took higher-resolution *H*-band spectra of some stars previously observed by SDSS/SEGUE, either serendipitously or deliberately targeted as part of a SEGUE overlap sample (Zasowski et al. 2013, 2017). APOGEE determined stellar parameters using the APOGEE Stellar Parameter and Chemical Abundances Pipeline, ASCAP (García Pérez et al. 2016). Holtzman et al. (2018) describe the ASPCAP results for DR14, including an assessment of their uncertainties and a description of the flags associated with data quality. To obtain a high-quality overlap sample, we eliminated stars from the APOGEE sample taken during commissioning observations or with the STAR_BAD flag set. In addition, because the APOGEE DR14 parameters are more uncertain for hot stars and rapidly rotating stars with weaker lines, we required that the APOGEE $T_{\rm eff} < 6000$ K and that the ROTATION_WARN flag was not set. For the SDSS/SEGUE stars, we required a valid TEFFADOP. This eliminated the M stars, for which the SSPP provides only spectral types. We eliminated duplicate observations in each survey by requiring the SDSS/SEGUE spectra to be the science_primary and by requiring that the APOGEE EXTRATARGET bit 4 flag was not set. These cuts resulted in a final sample of 571 stars. These stars, with their APOGEE and SSPP information, are listed in Table 9.

To compare the SSPP and ASPCAP parameters for each star, stars without a valid parameter measurement in both analyses were eliminated and a 3σ cut applied. The mean offset, rms, and number of stars ultimately used in the comparison of each parameter are compiled in Table 8 along with a summary of the results. The comparisons are shown in Figures 13 and 14.

We chose not to compare the SSPP $T_{\rm eff}$ values with APOGEE's because, as can be seen in Figure 13, most of the stars in common between the surveys are giants. This is problematic for two reasons: First, as described in Section 5.1, the SSPP's spectroscopic temperature indicator (TEFFSPEC), which dominates its TEFFADOP value, can be as much as 200 K hotter than the true IRFM value for giants. Second, the photometric TEFFIRFM indicator cannot be used because many of the stars in common between SEGUE and APOGEE have saturated SDSS photometry.

The log g mean offset is small, and the 0.25 dex rms scatter and the significant trend in log g between SSPP and ASPCAP is almost entirely due to systematic and random uncertainties in the SSPP measurements. The ASPCAP log g values have been shown to have uncertainties <0.1 dex when calibrated to log g measurements from asteroseismology (Holtzman et al. 2015). Gravities from SDSS/SEGUE are therefore sufficient to distinguish giants from dwarfs among the G and K stars (e.g., Schlesinger et al. 2012) but are not accurate enough for reliable luminosity estimates on their own (e.g., Xue et al. 2014). The results from the internal comparisons (see Figure 10 and Table 7) also indicate that uncertainties of at least 0.10–0.25 dex are expected. The systematic trends seen in

Table 9
Comparison of SSPP and ASPCAP Parameters (Abridged)

	SEGUE-2 Parameters				APOGEE-2 Parameters					
SPECOBJID	TEFFADOP (K)	LOGGADOP (cgs)	FEHADOP	ELODIERVFINAL (km s^{-1})	APOGEE_ID	TEFF (K)	LOGG (cgs)	FE_H	VHELIO_AVG (km s^{-1})	VSCATTER[a]
336684782110926848	5389.1	2.8	−1.7	151.0	2M13422183-0027007	5152.7	2.3	−1.9	154.0	1.7
459512328077993984	5237.5	2.6	−0.5	−22.7	2M02413544+0114311	5074.4	2.4	−0.7	−14.8	0.1
488665330206402560	4914.5	2.5	−0.3	10.3	2M07492407+4108331	4791.6	2.4	−0.2	12.7	0.2
489938564621035520	4851.5	2.6	0.1	33.8	2M07592374+4058530	4769.1	2.5	0.1	38.5	0.0
1102353356296316928	4701.3	1.8	−0.6	−47.9	2M17140124+2730297	4602.3	1.8	−0.8	−48.7	0.0
1177712784306104320	4256.5	3.8	−0.5	−3.0	2M14350795+4954080	3969.2	−9999.0	0.1	−2.7	0.5
1177769684032841728	5075.2	3.2	−1.5	−31.7	2M14244053+4929580	4025.0	−9999.0	−1.5	−39.9	0.6
1307287759815206912	4330.0	4.3	−1.0	−30.3	2M14245809+5612110	4340.0	−9999.0	−0.5	−32.3	0.3
1437901221020067840	5062.9	2.3	−0.6	−52.9	2M09500809+3851594	5057.4	2.4	−0.6	−56.6	0.3

Note.

[a] Column headings correspond to column names in the SDSS Catalog Archive Server ascapStar, apogeeStar, and sppParams database tables.

(This table is available in its entirety in machine-readable form.)
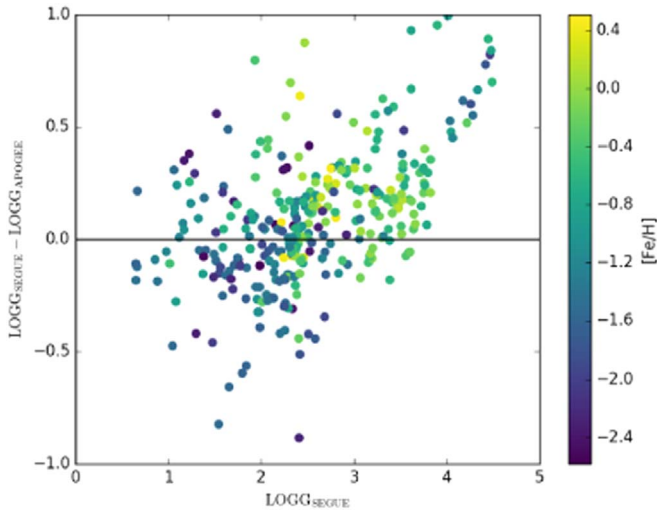
Figure 13. SEGUE vs. APOGEE log g comparison. Because ASPCAP DR14 did not provide calibrated values for dwarf stars, there are few stars in the sample with SSPP log $g > 4$, and those must have large differences between ASPCAP and the SSPP to make it into the sample. Therefore, we focus our attention on the comparison with the subgiant and giant log g measurements, where the mean offset is small. The SSPP log g values are useful for separating giants from dwarfs but not as accurate as the estimates from the higher-resolution APOGEE data. See also the discussion of Figure 9.
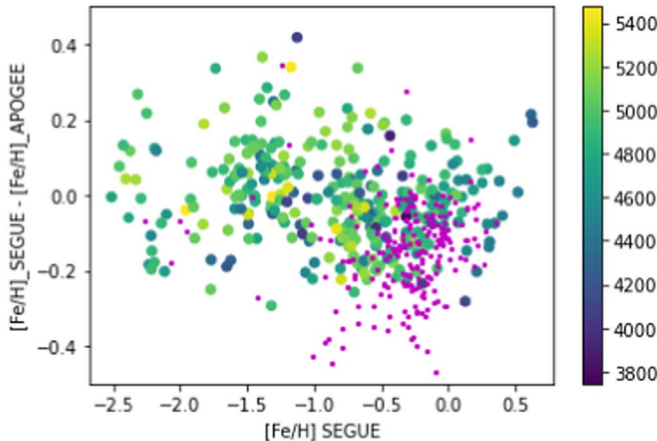
Figure 14. SEGUE vs. APOGEE [Fe/H] comparison. Dwarfs are shown as small magenta points, giants larger points color-coded by $T_{\rm eff}$. The comparison sample for giants spans a large range of [Fe/H]] and $T_{\rm eff}$ over which the offset is –0.06 and the scatter 0.15 dex. The only dwarf stars common between the surveys are metal rich and suggest that SSPP underestimates [Fe/H] for solar-metallicity dwarfs; see discussion of Figure 9.

the APOGEE comparison match the remaining residuals when comparing the final SSPP log g estimates to the values for the high-resolution sample (see Table 5 and discussion in Section 5.5) Note that for DR14, ASPCAP used log g values derived from asteroseismology (Holtzman et al. 2018) to calibrate giant stars; dwarf star log g values were not calibrated and are therefore not considered in the SSPP log g comparison.

To compare [Fe/H] estimates, Figure 14 plots [Fe/H] values for giants in the APOGEE−SEGUE overlap sample color-coded by $T_{\rm eff}$ and the dwarfs as small magenta points. The giants span a large range in [Fe/H], −2.5 to +0.5, and the mean offset is small, with scatter of 0.12 dex (see Table 8). The only dwarf stars in the APOGEE-SEGUE overlap sample are metal rich, with [Fe/H] $\gtrsim$ −0.2. The mean offset of this metal-rich dwarf sample is –0.15 dex with a scatter of 0.20 dex,

consistent with the offset of SSPP metallicities for stars with [Fe/H] > –0.2 in the right panel of Figure 9. Both the internal comparison (Table 7) and the ASPCAP comparison show that the uncertainties in the SSPP [Fe/H] values are ∼0.10–0.15 dex, depending on $T_{\rm eff}$ and metallicity. This is also consistent with the rms scatter of the cluster metallicity values, which include dwarfs at a range of metallicities (see Figure 11).

We also compared the RVs derived from the two surveys. For SDSS/SEGUE, we used the RV values derived by cross-correlating with templates from the high-resolution ELODIE survey (Moultaka et al. 2004), given in their final form as `ELODIERVFINAL` in the sppParams table. Their derivation, and an evaluation of the RV uncertainties, is discussed in detail in Yanny et al. (2009). Except for stars flagged as likely variables in APOGEE, the mean offset between the SDSS/ SEGUE and APOGEE RVs is only a few km s^{-1} and the rms scatter is 3.75 km s^{-1}. This APOGEE comparison is consistent with the RV uncertainties quoted in Yanny et al. (2009), but note that the SDSS/SEGUE RV uncertainties are a function of S/N; see Figure 2 and Table 2 of Yanny et al. (2009).

6.4. Caveats for the DR9 SSPP Parameters

When using the SSPP parameter table, some caution is required. Because of a mistake in the treatment of the inverse variance flux error array in the methods of `NGS1`, `NGS2`, and `CaIIK1`, there are a few stars with very incorrect parameters. Among all the SDSS/SEGUE spectra with valid $(g - r)_0$ and S/N limits for the SSPP, about 8280 (less than 2%) of the stars are affected by this minor bug in the SSPP. These stars can be removed by requiring the sppParam values for each star `CC_MGH > 0` and `CC_CAHK > 0`.

The log g values from the SSPP can have large (0.5–1.0 dex) systematic offsets, particularly for very cool giants and dwarfs. However, the SSPP log g estimates are clearly useful for separating dwarfs from giants in the GK spectral types. See Figure 13, Table 9, and the discussion in Schlesinger et al. (2012) and Xue et al. (2014).

7. From Spectroscopic Samples to Milky Way Populations

The SEGUE-2 spectroscopic survey, and the entire SDSS stellar spectroscopy sample, is most powerful for understanding the global properties of the Milky Way when used in conjunction with the SDSS *ugriz* imaging data from which all the spectroscopic targets were selected. The SDSS imaging data are essentially complete over the survey footprint in the magnitude range of the SEGUE spectroscopic sample. The USNO-B proper-motion data are available for the entire SDSS imaging footprint, and now the more accurate Gaia proper-motion and parallax data are available as well. The SEGUE-2 spectroscopy sparsely and unevenly samples the SDSS imaging data in stellar surface density, in color and magnitude, and in proper motion. To relate the properties of stars drawn from the SEGUE spectroscopic data to the Galaxy, it is necessary to correct for these subsampling factors.

A consequence of the premium on total area to maximize the number of distant halo tracers (Section 4) is that the survey observed each 7 deg^2 pointing only once, with just 640 fibers to allocate to spectroscopic targets. There are on average ∼7000 stars brighter than the SEGUE-2 magnitude limit at $g = 19.5$ in each 7 deg^2 field in the SDSS photometric footprint. Even at high Galactic latitudes, $b > 75°$, there are ∼5500 stars per field.

SEGUE-2, therefore, undersampled the sky by a factor that depends on Galactic latitude. The photometric and proper-motion selection criteria used to isolate particular types of stars cause more familiar observational biases, such as a bias toward metal-poor stars from a selection on ultraviolet color excess. A final consideration is that stars that fulfill multiple criteria for selection have multiple opportunities to be assigned a spectroscopic fiber, causing them to be overrepresented in the final sample. For example, SEGUE-1 used color and proper-motion selection to identify K-giant candidates. This selection criterion overlapped with the colors used to select K-dwarf stars. Thus, the raw spectroscopic K-dwarf category will have an over-abundance of low-proper -motion K-dwarf stars that meet the K-giant criteria. This same caution is relevant for the MSTO and high-velocity halo MSTO stars. This potential bias is less problematic for the other proper-motion-selected samples due to their small numbers and extreme criteria. The Gaia proper motions can be used to determine the actual proper-motion distribution of the SEGUE target samples much more accurately than was possible at the time of observation.

Below we summarize some common situations and point to examples in the literature of procedures to account for the selection biases.

1. If an individual object is of interest on its own, then the rest of this section can be safely ignored. For example, identification of individual candidate extremely metal-poor stars does not require correcting for the metallicity bias of the ultraviolet-excess selection of the metal-poor star candidates.

2. If it is important to determine why a star received a fiber, then the segue2_target1 flag in the specObjAll table has the relevant information, because only the bit for the target class that determined its place in the prioritized plate list is set. This flag is set based on the SEGUE-2 targeting photometry.

3. To determine which stars in an area observed by SEGUE-2 passed the targeting criteria in the photometry used to select the targets, the sppTargets table should be used. This table lists the targeting flags for all stars on the SEGUE-2 plates. Note that for objects actually observed by SEGUE-2, this same targeting information is also available as part of the data associated with each spectrum.

4. To determine which objects in the entire SDSS footprint meet any of the SEGUE-1 or SEGUE-2 targeting criteria, use the sequeTargetAll table. As mentioned above in Section 4, the final DR8 photometry is better calibrated and more homogeneous than the photometry available at the time of the SEGUE-2 observations. The SEGUE-1 and SEGUE-2 targeting code was rerun over the entire SDSS imaging footprint using the DR8 version of the photometry, allowing extrapolation of the observed spectroscopic samples to the entire SDSS footprint. This information is stored in the sequeTargetAll table. We recommend using this updated targeting information.

5. To use the SEGUE spectra to infer the properties of a Galactic population and if the SEGUE targets have been drawn randomly from stars within a single color and magnitude region, then techniques discussed in, e.g., Rix & Bovy (2013) and Bovy et al. (2014) can be used to recreate the underlying population from a magnitude-limited, undersampled survey. For example, Bovy et al. (2014) show how to compensate for the uneven sampling in magnitude of the APOGEE survey and match the spectroscopic sample to the photometric catalog from which it was drawn. None of the target categories in SEGUE-2 fully meet those criteria. Depending on the science case, the effects of overlapping target categories may be small enough to ignore or are not relevant to the actual analysis. In some cases, however, they will not be negligible, and additional corrections will be needed.

6. If overlapping selection criteria or biases in the sample due to selection criteria are not relevant to the analysis, then they do not have to be accounted for. An example is the Bovy et al. (2012) analysis of the spatial distribution of stellar populations as a function of their chemical abundance. They design the selection of their monoabundance populations to be sufficiently small regions of color and magnitude that the probability of a star being targeted is constant within one region. Their analysis looks at the relative spatial distribution of different monoabundance populations in the Milky Way disk, which is not affected by any absolute difference in the targeting probability between the monoabundance populations because it is constant for all SEGUE-1 and SEGUE-2 data.

7. To reconstruct the underlying distribution of a property of a population in cases where targeting classes significantly overlap and introduce biases in metallicity, Schlesinger et al. (2012) provide a description of how to do this using photometric information. They describe how to obtain the correct MDF for the G and K dwarfs from the SEGUE-1 spectroscopic sample. In brief, they use DR8 photometry to determine the number of stars in each of three overlapping target types within the $g - r$ limits of the G-dwarf and K-dwarf SEGUE-1 target categories. They compare them to the number of those candidates that have spectra to compute a weight for each overlap region. They then adjust the spectroscopic sample by these weights to remove the selection biases and recover the underlying population. Numerous other approaches could also be used, for example, forward modeling of the survey selection.

Appendix A
Target Selection for Rare Objects: The M Giants

When the objects that are targeted are very rare, we run into the situation where photometric errors in the colors used to select targets produce a large number of false targets. This can be illustrated clearly by taking a close look at the target selection for the M-giant class and in particular the difference it makes if post-DR8 photometry, which was improved when the "ubercalibration" technique (Padmanabhan et al. 2008) is used. Note that we have chosen to use the DR12 photometry, rather than later updates for SEGUE, because the vitally important cluster observations that were used to calibrate the photometry into physical quantities have not been transformed onto the Pan-STARRS calibrated photometric system.

The photometry used for the initial target selection for M giants, using pre-DR8 photometry, can be found by querying the sppTargets table, using the following query:

```
select gmr0,umg0,psfmag_g,psfmag_i,
   psfmagerr_g,psfmagerr_r,
   pmra,pmdec,pmsigra,pmsigdec,dist22,nfit,
   plate,mjd,fiberid
from sppTargets
   into myDB.mgitargphot
where segue2_target1 = -2147483520
```

The query returns 608 stars. A few of the stars were removed in the plate design stage because of fiber collisions, etc. We can find the actual number of M-giant targets observed in SEGUE-2 using the following query:

```
select s.plate,s.mjd,s.fiberid,
s.psfMag_g-s.extinction_g as g0, s.psfMag_g-extinc-
  tion_g-s.psfMag_r+extinction_r as gr0,
   s.psfMag_u-s.extinction_u-s.psfmag_g +extinction_g
  as ug0,
   l.NaI20side, s.ra,s.dec
into myDB.mgiantsobs
from SpecPhotoAll as s
   join sppLines as l
   on s.plate = l.plate and s.mjd = l.mjd and s.
  fiberid = l.fiber
where s.segue2_target1 = -2147483520
   and s.SciencePrimary = 1
```
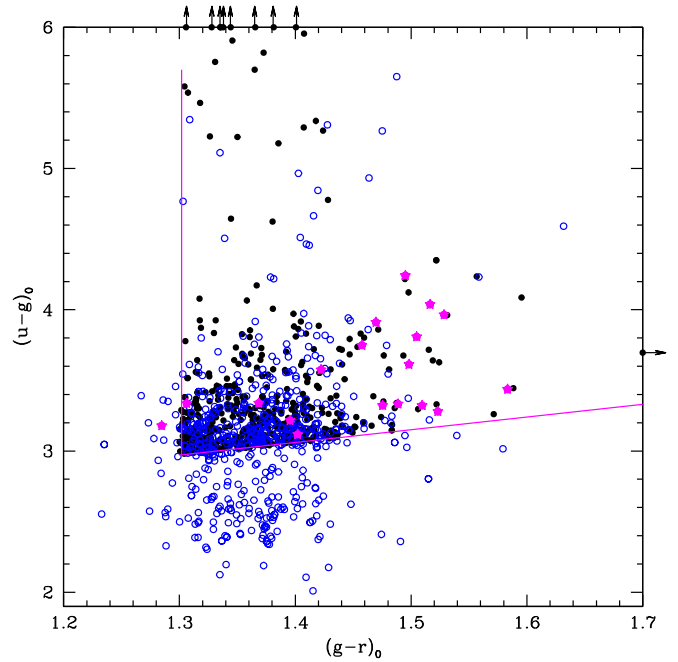

Figure A1. $(g - r)_0$ vs. $(u - g)_0$ diagram illustrating the effect of ubercalibration on the targeting of rare stars such as M giants in the halo. Black points show the (pre-DR8) photometry used in SEGUE-2 target selection; open blue points show the DR12 (ubercalibrated) photometry. It can be seen that many of the targets had extreme colors due to errors in the pre-DR8 photometry. Spectroscopically confirmed M giants are shown in magenta, and the M-giant selection box is outlined with a magenta line.

A total of 569 stars satisfied this query. It queries the table SpecPhotoAll for the magnitudes and position on the sky of all the M-giant targets and the sppLines table for the Na I line-index value for each star. Note the important requirement that only the best spectroscopic observation of each star be used, using the SciencePrimary flag. The query was executed in the DR12 environment and so returns the ubercalibrated photometry.

We see the advantage of ubercalibration, particularly in the u band, by matching the two lists of M-giant targets and comparing their photometry. We find that while the $g - r$ colors remained fairly unchanged, a remarkable 44% of the sample had a change in $u - g$ of 0.1 mag or more, and that there was also a zero-point shift: The median post-ubercalibration M-giant target colors were 0.08 mag bluer. This highlights the problem of selecting targets that have unusual colors: Many of the stars with large changes in $u - g$ had large color errors in the pre-DR8 photometry used for targeting, rather than being bona fide M-giant targets.

Figure A1 shows the change of colors described above. It can be seen that many of the ubercalibrated colors (shown in blue) are completely outside the selection box.

It is also interesting to inquire how many M-giant targets would have been produced if the ubercalibrated photometry had been used for the original target selection. This is made simple by using the SegueTargetAll table and matching with the footprint of the SEGUE-2 survey, as shown in the queries below.

First, the R.A. and decl. of all the SEGUE-2 plates is found by querying the PlateX table and putting the results into myDB.

```
select p.plate,p.mjd,p.ra,p.dec
into myDB.seg2platelist
from platex p
where survey = 'segue2'
order by ra
```

Then we search `SegueTargetAll` for all stars that satisfied the M-giant target criteria and were within the area of the SEGUE-2 plates:

```
SELECT
m.plate,m.mjd, m.ra AS ra1, m.dec AS dec1,
n.objid, n.distance, s.segue2_target1,
    o.ra AS ra2, o.dec AS dec2,
    o.psfmag_u---o.extinction_u---o.psfMag_g + o.
  extinction_g as ug0,
    o.psfmag_g-extinction_g-o.psfMag_r-o.extinction_r
  as gr0,o.psfmag_r-o.extinction_r as r0
into mydb.dr12mgiants
from MyDB.seg2platelist AS m
CROSS APPLY dbo.fGetNearbyObjAllEq(m.ra,m.dec,90) AS n
    JOIN PhotoObj AS o ON n.objid = o.objid
    JOIN seguetargetall as s on o.objid = s.objid
where segue2_target1 = -2147483520
and o.mode = 1
```

This query returns 886 objects. (Note the mode = 1 requirement for primary objects in PhotoObj.)

Appendix B
Changes Made to the DR9 SSPP

The reevaluation of the SSPP performance through comparisons with the higher-resolution optical spectra motivated several improvements to the individual SSPP estimators as well as to the final, weighted results for DR9. Below is an itemized list of the changes made in the DR9 SSPP since DR8.

1. `NGS1` and `CaIIK1` make use of a new grid of synthetic spectra generated with α-enhanced Kurucz model atmospheres, rather than just scaled-solar atmospheres (Lee et al. 2008a), and with microturbulence velocity a function of surface gravity. The adopted relation is $v_t = -0.345 \cdot \log g + 2.225$. This improves the metallicity estimates for cool, metal-rich stars.

2. `NGS2` also utilizes a new grid of synthetic spectra created with α-enhanced Kurucz model atmospheres and with microturbulence velocity fixed at $1\,km\,s^{-1}$, a more appropriate value for the main-sequence stars that make up a majority of the stars (e.g., Valenti & Fischer 2005; Holtzman et al. 2018)

3. The grid of synthetic spectra used in the `NGS1`, `CaIIK1`, and `NGS2` estimates is extended to [Fe/H] = −4.5 and [Fe/H] = +1.0 to improve the estimates at low metallicity and above solar metallicity.

4. The three photometric estimates of T_{eff} (T_K, T_G, and T_I) are replaced by the photometric temperature `TEFFIRFM` estimated using a color–T_{eff} relation based on an infrared flux method (IRFM) relation. This relation uses the $(g - i)_0$ color and iteratively accounts for the dependence on $\log g$ and [Fe/H].

5. For `k24`, `ki13`, `NGS1`, `NGS2`, and `CaIIK1`, cubic spline interpolation is used to interpolate the flux values in the grid of synthetic spectra for χ^2 minimization. This improves over the linear interpolation used in previous versions.

6. If more than 5% of a region of a spectrum used by a particular parameter estimation method has the inverse variance of the spectrum flux array set to zero (which happens, for example, in the case of missing data in the spectrum), no parameter estimate is reported for that particular method. This was done to improve the reliability of the parameter estimates, especially at very low metallicity.

7. A new set of $(g - r)_0$ and S/N limits was introduced for individual methods. These changes were made after evaluating the accuracy of the individual estimators in the SSPP for a set of synthetic spectra with realistic noise properties covering the range of $(g - r)_0$ and S/N in the SEGUE data, as well as the high-resolution and cluster spectra. See Lee et al. (2008a) for the details on the noise-injection experiment.

8. New neural networks trained on the new grid of synthetic spectra and the DR8 parameters are implemented for `ANNSR` and `ANNRR`, respectively. The `ANNSR` estimate no longer contributes to the adopted metallicity estimates.

9. Metallicity estimates from autocorrelation Function (ACF) and Ca II triplet line-index (`CaIIT`) methods are longer reported and do not contribute to the adopted metallicity estimate for each star.

10. Gravity estimates from the `MgH` and `CaI2` line-index methods and `k24` are no longer reported and do not contribute to the best gravity estimate for each star.

B.1. New $(g - r)_0$ and S/N Limits for Individual Methods

The S/N and $(g - r)_0$ limits were also revised for DR9 according to new experiments that add realistic noise to synthetic spectra and SDSS/SEGUE spectra for which we have high-resolution calibration spectra. This noise-injection experiment technique is described in Lee et al. (2008a), and the interested reader is referred to the paper. Table 3 summarizes the adopted ranges of S/N and $(g - r)_0$ for each method used in the SSPP.

ORCID iDs

Constance M. Rockosi ⓘ https://orcid.org/0000-0002-6667-7028
Young Sun Lee ⓘ https://orcid.org/0000-0001-5297-4518
Brian Yanny ⓘ https://orcid.org/0000-0002-9541-2678
Jennifer A. Johnson ⓘ https://orcid.org/0000-0001-7258-1834
Jennifer Sobeck ⓘ https://orcid.org/0000-0002-4989-0353
Timothy C. Beers ⓘ https://orcid.org/0000-0003-4573-6233
Carlos Allende Prieto ⓘ https://orcid.org/0000-0002-0084-572X
Deokkeun An ⓘ https://orcid.org/0000-0002-8072-7511
Dmitry Bizyaev ⓘ https://orcid.org/0000-0002-3601-133X
Michael R. Blanton ⓘ https://orcid.org/0000-0003-1641-6222
Luca Casagrande ⓘ https://orcid.org/0000-0003-2688-7511
Daniel J. Eisenstein ⓘ https://orcid.org/0000-0002-2929-3121
H. R. Jacobson ⓘ https://orcid.org/0000-0001-7727-1640
Gillian R. Knapp ⓘ https://orcid.org/0000-0002-9259-1164
Juna A. Kollmeier ⓘ https://orcid.org/0000-0001-9852-1610
Sébastien Lépine ⓘ https://orcid.org/0000-0002-2437-2947
Martín López-Corredoira ⓘ https://orcid.org/0000-0001-6128-6274

Heidi J. Newberg ⓘ https://orcid.org/0000-0001-8348-0983
Kaike Pan ⓘ https://orcid.org/0000-0002-2835-2556
Conor Sayers ⓘ https://orcid.org/0000-0002-4454-1920
David H. Weinberg ⓘ https://orcid.org/0000-0001-7775-7261

References

Abadi, M. G., Navarro, J. F., Fardal, M., Babul, A., & Steinmetz, M. 2010, MNRAS, 407, 435
Abolfathi, B., Aguado, D. S., Aguilar, G., et al. 2018, ApJS, 235, 42
Ahn, C. P., Alexandroff, R., Prieto, C. A., et al. 2012, ApJS, 203, 21
Aihara, H., Allende Prieto, C., An, D., et al. 2011, ApJS, 193, 29
Albareti, F. D., Allende Prieto, C., Almeida, A., et al. 2017, ApJS, 233, 25
Allende Prieto, C., Beers, T. C., Wilhelm, R., et al. 2006, ApJ, 636, 804
Allende-Prieto, C., Sivarani, T., Beers, T. C., et al. 2008, AJ, 136, 2070
Alonso, A., Arribas, S., & Martínez-Roger, C. 1996, A&AS, 117, 227
An, D., & Beers, T. C. 2020, ApJ, 897, 39
An, D., & Beers, T. C. 2021, ApJ, 907, 101
An, D., Beers, T. C., Johnson, J. A., et al. 2013, ApJ, 763, 65
An, D., Beers, T. C., Santucci, R. M., et al. 2015, ApJL, 813, L28
An, D., Johnson, J. A., Clem, J. L., et al. 2008, ApJS, 179, 326
Aoki, W., Beers, T. C., Honda, S., & Carollo, D. 2010, ApJL, 723, L201
Aoki, W., Beers, T. C., Lee, Y. S., et al. 2012, AJ, 145, 13
Aoki, W., Suda, T., Beers, T. C., & Honda, S. 2015, AJ, 149, 39
Aoki, W., Tominaga, N., Beers, T. C., Honda, S., & Lee, Y. S. 2014, Sci, 345, 912
Asplund, M., & García Pérez, A. E. 2001, A&A, 372, 601
Barklem, P. S., Christlieb, N., Beers, T. C., et al. 2005, A&A, 439, 129
Battaglia, G., Helmi, A., Morrison, H., et al. 2005, MNRAS, 364, 433
Beers, T. C., Carollo, D., Ivezić, Ž., et al. 2012, ApJ, 746, 34
Beers, T. C., & Christlieb, N. 2005, ARA&A, 43, 531
Beers, T. C., Preston, G. W., & Shectman, S. A. 1985, AJ, 90, 2089
Beers, T. C., Preston, G. W., & Shectman, S. A. 1992, AJ, 103, 1987
Beers, T. C., Rossi, S., Norris, J. E., Ryan, S. G., & Shefler, T. 1999, AJ, 117, 981
Bell, E. F., Zucker, D. B., Belokurov, V., et al. 2008, ApJ, 680, 295
Belokurov, V, Deason, A J, Koposov, S E, et al. 2018a, MNRAS, 477, 1472
Belokurov, V., Erkal, D., Evans, N. W., Koposov, S. E., & Deason, A. J. 2018b, MNRAS, 478, 611
Belokurov, V., Koposov, S. E., Evans, N. W., et al. 2014, MNRAS, 437, 116
Belokurov, V., Sanders, J. L., Fattahi, A., et al. 2020, MNRAS, 494, 3880
Belokurov, V., Zucker, D. B., Evans, N. W., et al. 2006, ApJL, 642, L137
Bird, S. A., Xue, X.-X., Liu, C., et al. 2019, AJ, 157, 104
Blackwell, D. E., Petford, A. D., & Shallis, M. J. 1980, A&A, 82, 249
Blackwell, D. E., & Shallis, M. J. 1977, MNRAS, 180, 177
Blanton, M. R., Bershady, M. A., Abolfathi, B., et al. 2017, AJ, 154, 28
Bonaca, A., Conroy, C., Wetzel, A., Hopkins, P. F., & Kereš, D. 2017, ApJ, 845, 101
Bond, H. E. 1980, ApJS, 44, 517
Bonifacio, P., Caffau, E., Spite, M., et al. 2015, A&A, 579, A28
Boubert, D., Guillochon, J., Hawkins, K., et al. 2018, MNRAS, 479, 2789
Bovy, J., Nidever, D. L., Rix, H.-W., et al. 2014, ApJ, 790, 127
Bovy, J., Rix, H.-W., Liu, C., et al. 2012, ApJ, 753, 148
Boylan-Kolchin, M., Springel, V., White, S. D. M., & Jenkins, A. 2010, MNRAS, 406, 896
Bressan, A., Marigo, P., Girardi, L., et al. 2012, MNRAS, 427, 127
Brown, W. R., Geller, M. J., & Kenyon, S. J. 2014, ApJ, 787, 89
Brown, W. R., Geller, M. J., Kenyon, S. J., & Kurtz, M. J. 2005, ApJL, 622, L33
Caffau, E., Bonifacio, P., François, P., et al. 2011, Natur, 477, 67
Caffau, E., Bonifacio, P., Sbordone, L., et al. 2013, A&A, 560, A71
Callingham, T. M., Cautun, M., Deason, A. J., et al. 2019, MNRAS, 484, 5453
Carney, B. W., Laird, J. B., Latham, D. W., & Aguilar, L. A. 1996, AJ, 112, 668
Carollo, D., Beers, T. C., Bovy, J., et al. 2011, ApJ, 744, 195
Carollo, D., Beers, T. C., Chiba, M., et al. 2010, ApJ, 712, 692
Carollo, D., Beers, T. C., Lee, Y. S., et al. 2007, Natur, 450, 1020
Casagrande, L., Portinari, L., & Flynn, C. 2006, MNRAS, 373, 13
Casagrande, L., Ramírez, I., Meléndez, J., Bessell, M., & Asplund, M. 2010, A&A, 512, A54
Casagrande, L., Wolf, C., Mackey, A. D., et al. 2019, MNRAS, 482, 2770
Cheng, J. Y., Rockosi, C. M., Morrison, H. L., et al. 2012, ApJ, 746, 149
Chiba, M., & Beers, T. C. 2000, AJ, 119, 2843
Clewley, L., Warren, S. J., Hewett, P. C., et al. 2002, MNRAS, 337, 87

Cohen, J. G., Briley, M. M., & Stetson, P. B. 2005, AJ, 130, 1177
Cohen, J. G., Christlieb, N., Thompson, I., et al. 2013, ApJ, 778, 56
Conroy, C., Bonaca, A., Cargile, P., et al. 2019a, ApJ, 883, 107
Conroy, C., Naidu, R. P., Zaritsky, D., et al. 2019b, ApJ, 887, 237
Cooper, A. P., Cole, S., Frenk, C. S., et al. 2010, MNRAS, 406, 744
Cunningham, E. C., Deason, A. J., Sanderson, R. E., et al. 2019, ApJ, 879, 120
Dawson, K. S., Schlegel, D. J., Ahn, C. P., et al. 2013, AJ, 145, 10
de Jong, J. T. A., Yanny, B., Rix, H.-W., et al. 2010, ApJ, 714, 663
de la Fuente Marcos, R., & de la Fuente Marcos, C. 2019, A&A, 627, A104
De Silva, G. M., Freeman, K. C., Bland-Hawthorn, J., et al. 2015, MNRAS, 449, 2604
Deason, A. J., Belokurov, V., & Evans, N. W. 2010, MNRAS, 411, 1480
Deason, A. J., Belokurov, V., & Evans, N. W. 2011, MNRAS, 416, 2903
Deason, A. J., Belokurov, V., Evans, N. W., & An, J. 2012, MNRAS: Letters, 424, L44
Deason, A. J., Van der Marel, R. P., Guhathakurta, P., Sohn, S. T., & Brown, T. M. 2013, ApJ, 766, 24
Dekker, H., D'Odorico, S., Kaufer, A., Delabre, B., & Kotzlowski, H. 2000, Proc. SPIE, 4008, 534
Dohm-Palmer, R. C., Helmi, A., Morrison, H., et al. 2001, ApJL, 555, L37
Dong, R., Gunn, J., Knapp, G., Rockosi, C., & Blanton, M. 2011, AJ, 142, 116
Du, C., Li, H., Yan, Y., et al. 2019, ApJS, 244, 4
Eggen, O. J., Lynden-Bell, D., & Sandage, A. R. 1962, ApJ, 136, 748
Eisenstein, D. J., Weinberg, D. H., Agol, E., et al. 2011, AJ, 142, 72
El-Badry, K., Bland-Hawthorn, J., Wetzel, A., et al. 2018, MNRAS, 480, 652
Fermani, F., & Schönrich, R. 2013, MNRAS, 432, 2402
Fernández-Alvar, E., Allende Prieto, C., Beers, T. C., et al. 2016, A&A, 593, A28
Fernández-Alvar, E., Tissera, P. B., Carigi, L., et al. 2019, MNRAS, 485, 1745
Finkbeiner, D. P., Schlafly, E. F., Schlegel, D. J., et al. 2016, ApJ, 822, 66
Fiorentin, P. R., Bailer-Jones, C. A. L., Lee, Y. S., et al. 2007, A&A, 467, 1373
Gaia Collaboration, Helmi, A., van Leeuwen, F., et al. 2018, A&A, 616, A12
García Pérez, A. E., Allende Prieto, C., Holtzman, J. A., et al. 2016, AJ, 151, 144
Gilbert, K. M., Guhathakurta, P., Kalirai, J. S., et al. 2006, ApJ, 652, 1188
Gilmore, G., Randich, S., Asplund, M., et al. 2012, Msngr, 147, 25
Gizis, J. E. 1997, AJ, 113, 806
Gray, D. F. 2008, The Observation and Analysis of Stellar Photospheres (Cambridge: Cambridge Univ. Press)
Gunn, J. E., Siegmund, W. A., Mannery, E. J., et al. 2006, AJ, 131, 2332
Hansen, T. T., Holmbeck, E. M., Beers, T. C., et al. 2018, ApJ, 858, 92
Harrigan, M. J., Newberg, H. J., Newberg, L. A., et al. 2010, MNRAS, 405, 1796
Hattori, K., Valluri, M., Loebman, S. R., & Bell, E. F. 2017, ApJ, 841, 91
Hawkins, K., & Wyse, R. F. G. 2018, MNRAS, 481, 1028
Hayes, C. R., Majewski, S. R., Shetrone, M., et al. 2018, ApJ, 852, 49
Helmi, A. 2008, A&ARv, 15, 145
Helmi, A., Babusiaux, C., Koppelman, H. H., et al. 2018, Natur, 563, 85
Helmi, A., Navarro, J. F., Meza, A., Steinmetz, M., & Eke, V. R. 2003, ApJL, 592, L25
Hills, J. G. 1988, Natur, 331, 687
Holtzman, J. A., Hasselquist, S., Shetrone, M., et al. 2018, AJ, 156, 125
Holtzman, J. A., Shetrone, M., Johnson, J. A., et al. 2015, AJ, 150, 148
Huang, Y., Beers, T. C., Wolf, C., et al. 2021, ApJ, 925, 164
Ibata, R. A., Gilmore, G., & Irwin, M. J. 1994, Natur, 370, 194
Ibata, R. A., Irwin, M. J., Lewis, G. F., Ferguson, A. M. N., & Tanvir, N. 2003, MNRAS, 340, L21
Ivezić, Ž., Sesar, B., Jurić, M., et al. 2008, ApJ, 684, 287
Ivezić, Ž., Smith, J. A., Miknaitis, G., et al. 2007, AJ, 134, 973
Jackson-Jones, R., Jofré, P., Hawkins, K., et al. 2014, A&A, 571, L5
Janesh, W., Morrison, H. L., Ma, Z., et al. 2016, ApJ, 816, 80
Johnston, K. V., Bullock, J. S., Sharma, S., et al. 2008, ApJ, 689, 936
Kafle, P. R., Sharma, S., Lewis, G. F., & Bland-Hawthorn, J. 2012, ApJ, 761, 98
Karademir, G. S., Remus, R.-S., Burkert, A., et al. 2019, MNRAS, 487, 318
Kenyon, S. J., Bromley, B. C., Brown, W. R., & Geller, M. J. 2018, ApJ, 864, 130
Kilic, M., Munn, J. A., Harris, H. C., et al. 2006, AJ, 131, 582
Kollmeier, J. A., & Gould, A. 2007, ApJ, 664, 343
Kollmeier, J. A., Gould, A., Knapp, G., & Beers, T. C. 2009, ApJ, 697, 1543
Kollmeier, J. A., Gould, A., Rockosi, C., et al. 2010, ApJ, 723, 812
Koposov, S. E., Boubert, D., Li, T. S., et al. 2020, MNRAS, 491, 2465
Kraft, R. P. 1994, PASP, 106, 553
Lai, D. K., Bolte, M., Johnson, J. A., et al. 2008, ApJ, 681, 1524
Lee, Y. S., Beers, T. C., & Kim, Y. K. 2019, ApJ, 885, 102
Lee, Y. S., Beers, T. C., Masseron, T., et al. 2013, AJ, 146, 132

Lee, Y. S., Beers, T. C., Sivarani, T., et al. 2008a, AJ, 136, 2022
Lee, Y. S., Beers, T. C., Sivarani, T., et al. 2008b, AJ, 136, 2050
Lenz, D. D., Newberg, J., Rosner, R., Richards, G. T., & Stoughton, C. 1998, ApJS, 119, 121
Lepine, S., Rich, R. M., & Shara, M. M. 2007, ApJ, 669, 1235
Lépine, S., & Scholz, R.-D. 2008, ApJL, 681, L33
Lépine, S., Shara, M. M., & Rich, R. M. 2002, AJ, 124, 1190
Li, H.-N., Aoki, W., Honda, S., et al. 2015a, RAA, 15, 1264
Li, H.-N., Zhao, G., Christlieb, N., et al. 2015b, ApJ, 798, 110
López-Corredoira, M., & Molgó, J. 2014, A&A, 567, A106
Ludwig, H. G., Bonifacio, P., Caffau, E., et al. 2008, PhST, 133, 014037
Luo, A. L., Chen, J.-J., Hou, W., et al. 2018, Proc. SPIE, 10707, 107072B
Luo, A. L., Zhao, Y.-H., Zhao, G., et al. 2015, RAA, 15, 1095
Majewski, S. R. 1993, ARA&A, 31, 575
Majewski, S. R., Kunkel, W. E., Law, D. R., et al. 2004, AJ, 128, 245
Majewski, S. R., Schiavon, R. P., Frinchaboy, P. M., et al. 2017, AJ, 154, 94
Marchetti, T., Rossi, E. M., & Brown, A. G. A. 2019, MNRAS, 490, 157
Martell, S. L., Sharma, S., Buder, S., et al. 2017, MNRAS, 465, 3203
Mateo, M., Olszewski, E. W., & Morrison, H. L. 1998, ApJL, 508, L55
McWilliam, A., Preston, G. W., Sneden, C., & Searle, L. 1995, AJ, 109, 2757
Monachesi, A., Gómez, F. A., Grand, R. J. J., et al. 2019, MNRAS, 485, 2589
Monari, G., Famaey, B., Carrillo, I., et al. 2018, A&A, 616, L9
Monet, D. G., Levine, S. E., Canzian, B., et al. 2003, AJ, 125, 984
Morrison, H. L., Ma, Z., Clem, J. L., et al. 2016, AJ, 151, 7
Moultaka, J., Ilovaisky, S. A., Prugniel, P., & Soubiran, C. 2004, PASP, 116, 693
Munn, J. A., Monet, D. G., Levine, S. E., et al. 2004, AJ, 127, 3034
Naidu, R. P., Conroy, C., Bonaca, A., et al. 2020, ApJ, 901, 48
Newberg, H. J., Yanny, B., Grebel, E. K., et al. 2003, ApJL, 596, L191
Newberg, H. J., Yanny, B., Rockosi, C., et al. 2002, ApJ, 569, 245
Nissen, P. E., & Schuster, W. J. 2010, A&A, 511, L10
Noguchi, K., Aoki, W., Kawanomoto, S., et al. 2002, PASJ, 54, 855
Norris, J. E., Ryan, S. G., & Beers, T. C. 1999, ApJS, 123, 639
Padmanabhan, N., Schlegel, D. J., Finkbeiner, D. P., et al. 2008, ApJ, 674, 1217
Pier, J. R. 1983, ApJS, 53, 791
Piffl, T., Scannapieco, C., Binney, J., et al. 2014, A&A, 562, A91
Placco, V. M., Frebel, A., Beers, T. C., & Stancliffe, R. J. 2014, ApJ, 797, 21
Queiroz, A. B. A., Anders, F., Santiago, B. X., et al. 2018, MNRAS, 476, 2556
Ramírez, I., & Meléndez, J. 2004, A&A, 417, 301
Rix, H.-W., & Bovy, J. 2013, A&ARv, 21, 61
Ruhland, C., Bell, E. F., Rix, H.-W., & Xue, X.-X. 2011, ApJ, 731, 119
Ryan, S. G., & Norris, J. E. 1991, AJ, 101, 1865
Santucci, R. M., Beers, T. C., Placco, V. M., et al. 2015a, ApJL, 813, L16
Santucci, R. M., Placco, V. M., Rossi, S., et al. 2015b, ApJ, 801, 116
Schiavon, R. P., & Barbuy, B. 1999, ApJ, 510, 934
Schlaufman, K. C., & Casey, A. R. 2014, ApJ, 797, 13
Schlegel, D. J., Finkbeiner, D. P., & Davis, M. 1998, ApJ, 500, 525
Schlesinger, K. J., Johnson, J. A., Rockosi, C. M., et al. 2012, ApJ, 761, 160
Searle, L., & Zinn, R. 1978, ApJ, 225, 357
Sheinis, A. I., Bolte, M., Epps, H. W., et al. 2002, PASP, 114, 851
Siegel, M. H., Dotter, A., Majewski, S. R., et al. 2007, ApJL, 667, L57

Sirko, E., Goodman, J., Knapp, G. R., et al. 2004a, AJ, 127, 914
Sirko, E., Goodman, J., Knapp, G. R., et al. 2004b, AJ, 127, 899
Smee, S. A., Gunn, J. E., Uomoto, A., et al. 2013, AJ, 146, 32
Smith, G. H., & Briley, M. M. 2006, PASP, 118, 740
Smith, M. C., Ruchti, G. R., Helmi, A., et al. 2007, MNRAS, 379, 755
Smolinski, J. P., Martell, S. L., Beers, T. C., & Lee, Y. S. 2011, AJ, 142, 126
Sneden, C., McWilliam, A., Preston, G. W., et al. 1996, ApJ, 467, 819
Sneden, C. A. 1973, PhD thesis, The University of Texas at Austin
Sobeck, J. S., Kraft, R. P., Sneden, C., et al. 2011, AJ, 141, 175
Starkenburg, E., Helmi, A., Morrison, H. L., et al. 2009, ApJ, 698, 567
Starkenburg, E., Oman, K. A., Navarro, J. F., et al. 2017, MNRAS, 465, 2212
Steinmetz, M., Zwitter, T., Siebert, A., et al. 2006, AJ, 132, 1645
Stonkutė, E., Koposov, S. E., Howes, L. M., et al. 2016, MNRAS, 460, 1131
Stoughton, C., Lupton, R. H., Bernardi, M., et al. 2002, AJ, 123, 485
Taylor, C., Boylan-Kolchin, M., Torrey, P., Vogelsberger, M., & Hernquist, L. 2016, MNRAS, 461, 3483
Tissera, P. B., Beers, T. C., Carollo, D., & Scannapieco, C. 2014, MNRAS, 439, 3128
Tull, R. G. 1998, Proc. SPIE, 3355, 387
Tumlinson, J. 2010, ApJ, 708, 1398
Turnshek, D. E., Turnshek, D. A., Craine, E. E., & Boeshaar, P. C. 1985, An Atlas of Digital Spectra of Cool Stars (Tucson, AZ: Western Research Company)
Valenti, J. A., & Fischer, D. A. 2005, ApJS, 159, 141
Vickers, J. J., Grebel, E. K., & Huxor, A. P. 2012, AJ, 143, 86
Vickers, J. J., Smith, M. C., & Grebel, E. K. 2015, AJ, 150, 77
Vivas, A. K., & Zinn, R. 2006, AJ, 132, 714
Wang, J., Frenk, C. S., Navarro, J. F., Gao, L., & Sawala, T. 2012, MNRAS, 424, 2715
Whitten, D. D., Beers, T. C., Placco, V. M., et al. 2019, ApJ, 884, 67
Wilhelm, R., Beers, T. C., & Gray, R. O. 1999, AJ, 117, 2308
Williams, A. A., Belokurov, V., Casey, A. R., & Evans, N. W. 2017, MNRAS, 468, 2359
Wilson, J. C., Hearty, F. R., Skrutskie, M. F., et al. 2019, PASP, 131, 055001
Xu, Y., Newberg, H. J., Carlin, J. L., et al. 2015, ApJ, 801, 105
Xue, X.-X., Ma, Z., Rix, H.-W., et al. 2014, ApJ, 784, 170
Xue, X.-X., Rix, H.-W., Ma, Z., et al. 2015, ApJ, 809, 144
Xue, X. X., Rix, H. W., Zhao, G., et al. 2008, ApJ, 684, 1143
Yang, C., Xue, X.-X., Li, J., et al. 2019, ApJ, 880, 65
Yanny, B., Newberg, H. J., Grebel, E. K., et al. 2003, ApJ, 588, 824
Yanny, B., Rockosi, C., Newberg, H. J., et al. 2009, AJ, 137, 4377
Yoon, J., Beers, T. C., Dietz, S., et al. 2018, ApJ, 861, 146
Yoon, J., Beers, T. C., Placco, V. M., et al. 2016, ApJ, 833, 20
Zasowski, G., Cohen, R. E., Chojnowski, S. D., et al. 2017, AJ, 154, 198
Zasowski, G., Johnson, J. A., Frinchaboy, P. M., et al. 2013, AJ, 146, 81
Zhai, M., Xue, X.-X., Zhang, L., et al. 2018, RAA, 18, 113
Zhao, G., Zhao, Y.-H., Chu, Y.-Q., Jing, Y.-P., & Deng, L.-C. 2012, RAA, 12, 723
Zheng, Z., Carlin, J. L., Beers, T. C., et al. 2014, ApJL, 785, L23
Zolotov, A., Willman, B., Brooks, A. M., et al. 2009, ApJ, 702, 1058